Title

Oncogene-regulated release of extracellular vesicles

Journal

Developmental Cell, 56(13)

ISSN

1534-5807

Authors

Kilinc, Seda
Paisner, Rebekka
Camarda, Roman
et al.

Publication Date

2021-07-01

DOI

10.1016/j.devcel.2021.05.014

Published in final edited form as:

Dev Cell. 2021 July 12; 56(13): 1989–2006.e6. doi:10.1016/j.devcel.2021.05.014.

Oncogene Regulated Release of Extracellular Vesicles

Seda Kilinc[1,*], **Rebekka Paisner**[1,7], **Roman Camarda**[1,2,8], **Suprit Gupta**[3], **Olga Momcilovic**[1,9], **Rebecca A. Kohnz**[4,10], **Baris Avsaroglu**[1], **Noelle D. L'Etoile**[1], **Rushika M. Perera**[3,5], **Daniel K. Nomura**[4], **Andrei Goga**[1,5,6,11,*]

[1]Department of Cell & Tissue Biology, University of California, San Francisco, San Francisco, CA 94143, USA

[2]Biomedical Sciences Graduate Program, University of California, San Francisco, San Francisco, CA 94143, USA

[3]Department of Anatomy, University of California, San Francisco, San Francisco, CA 94143, USA

[4]Departments of Chemistry and Nutritional Sciences and Toxicology, University of California, Berkeley, Berkeley, CA 94720, USA

[5]Helen Diller Family Comprehensive Cancer Center, University of California, San Francisco, San Francisco, CA 94143, USA

[6]Department of Medicine, University of California, San Francisco, San Francisco, CA 94143, USA

[7]Present Address: Department of Biology, Johns Hopkins University, Baltimore, MD 21218, USA

[8]Present Address: Aquilo Capital Management, 1 Letterman Drive, San Francisco, CA 94129, USA

[9]Present Address: Regulatory Professionals, 8000 Jarvis Ave, Newark, CA 94560, USA

[10]Present Address: Merck Research Laboratories, 213 E Grand Ave, South San Francisco, CA, 94080, USA

[11]Lead Contact

SUMMARY

Oncogenes can alter metabolism by changing the balance between anabolic and catabolic processes. However, how oncogenes regulate tumor cell biomass remains poorly understood. Using isogenic MCF10A cells transformed with nine different oncogenes, we show that specific

[*]Correspondence to: seda.kilinc@ucsf.edu & andrei.goga@ucsf.edu.

AUTHOR CONTRIBUTIONS

All authors listed, have made substantial, direct, and intellectual contribution to the work, and approved it for publication. S.K. and A.G. conceived the study, designed the experiments and wrote the manuscript. S.K. led the research efforts and carried out most of the experiments. R.P. and O.M. helped particle tracking experiments. R.C., and R.A.K. performed metabolomic experiments and analysis. S.G. performed magic red and lysotracker experiments. B.A. helped with cancer cell line analysis. R.M.P. advised experiments. N.D.L. assisted with data analysis and writing. D.N. supervised metabolomic analysis. A.G. supervised the work.

DECLARATION OF INTERESTS The authors declare no competing interests.

oncogenes reduce the biomass of cancer cells by promoting EV release. While MYC and AURKB elicited the highest number of EVs, each oncogene selectively altered the protein composition of released EVs. Likewise, oncogenes alter secreted miRNAs. MYC overexpressing cells require ceramide, while AURKB require ESCRT to release high levels of EVs. We identify an inverse relationship between MYC upregulation and activation of the RAS/MEK/ERK signaling pathway for regulating EV release in some tumor cells. Finally, lysosome genes and activity are downregulated in the context of MYC and AURKB, suggesting that cellular contents instead of being degraded, were released via EVs. Thus, oncogene mediated biomass regulation via differential EV release is a new metabolic phenotype.

Graphical Abstract

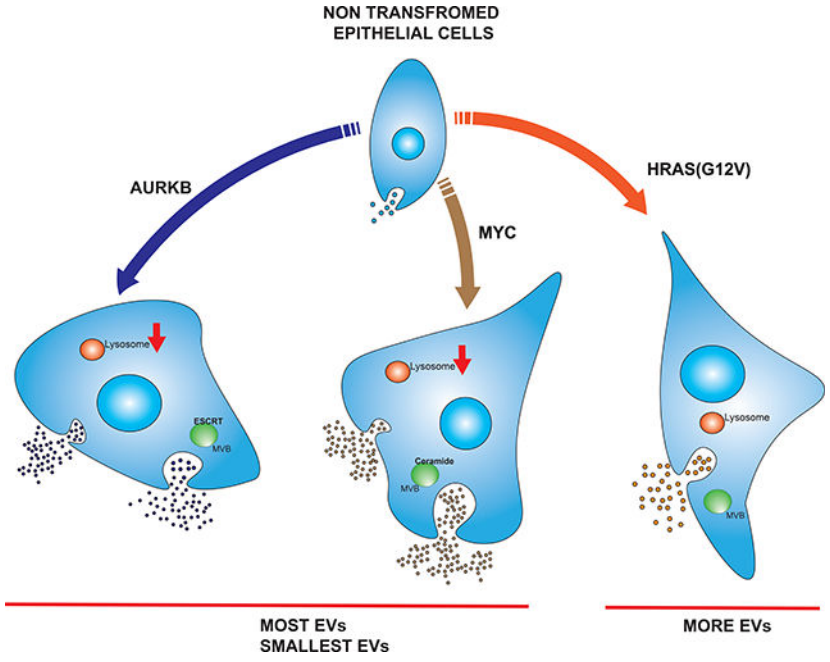

eTOC Blurb

Kilinc et. al. demonstrate that oncogenes alter released vesicle number and size as well as their heterogeneity. Oncogenes alter ceramide and ESCRT pathways involved in sEV production. MYC and AURKB oncogenes downregulate lysosome pathway and utilize EV release to maintain cellular homeostasis.

INTRODUCTION

Cancer cells reprogram metabolic processes to accommodate nutrient availability, energy needs and biosynthetic activity to support cell survival under stressful conditions or to increase biomass to support their proliferation (DeBerardinis and Chandel, 2016). Tumors frequently have mutations in PI3K and AKT oncogenes which result in aberrant activation of mTORC1 pathway that induce an anabolic growth resulting in nucleotide, protein and lipid synthesis (Yuan and Cantley, 2008). Likewise, MYC increases anabolic growth by altering genes involved in glycolysis, fatty acid synthesis, glutaminolysis, and serine

metabolism (Stine et al., 2015). When nutrients are limited, however, tumor cells activate catabolic pathways like fatty acid oxidation (FAO) to increase ATP levels (DeBerardinis and Chandel, 2016). MYC high triple negative breast (TNBC) cancer cells rely, in part, on FAO to fuel bioenergetic metabolism (Camarda et al., 2016). Likewise, intercellular proteins and other macromolecules can be recycled via autophagy to maintain pools of metabolic intermediates (Galluzzi et al., 2014). Alternatively, cancer cells can internalize proteins and other macromolecules from the tumor microenvironment via macropinocytosis (Commisso et al., 2013). In contrast, cells can lose biomass through extracellular vesicle (EV) release. Biomass loss via EV release is a facet of cancer metabolism that has not been explored in the context of specific transforming oncogenes.

EVs are secreted lipid bilayer membrane enclosed vesicles which contain proteins, lipids, RNA and DNA (Minciacchi et al., 2015). EVs are characterized with respect to their size, biogenesis, and content. Every cell secretes heterogenous populations of EVs ranging in size and differing in their biogenesis. Largest in size are the >1000 nm apoptotic bodies secreted from dying cells, which contain histones and fragmented DNA. The 100–1000nm, large EVs, generally termed microvesicles (MVs), are formed by blebbing of plasma membranes. Exosomes, small ~ 30–150nm EVs originate by inward budding of endosomal membranes into multivesicular bodies (MVBs) and are released as MVBs fuse with the plasma membrane (Bebelman et al., 2018; Colombo et al., 2014; Gustafson et al., 2017). Recent studies have also identified secreted non-membranous nanoparticles (<50nm), called exomeres, that are enriched in metabolic enzymes, cytoskeleton and Ago proteins (Jeppesen et al., 2019; Zhang et al., 2018a, 2019).

Cancer cells can release EVs to reshape the tumor microenvironment by triggering angiogenesis, permitting immune surveillance escape or alter the behavior of surrounding cells (Becker et al., 2016; Desrochers et al., 2016; Kalluri, 2016; Poggio et al., 2019). The function of EVs in cancer development and progression and their potential use as biomarkers or vehicles for drug therapy is under investigation (Andaloussi et al., 2013; Kalluri, 2016; Sousa et al., 2015). miRNAs are frequently identified EV cargos which may function to reprogram the recipient cells; for example exosomal miRNAs secreted by metastatic breast cancer cells target tight junction protein expression and destroy vascular endothelial barriers of surrounding cells, promoting migration and metastasis (Zhou et al., 2014). Alternatively, cancer cells can utilize EVs to secrete tumor suppressive miRNAs and toxic lipids to favor tumor growth (Kanlikilicer et al., 2016).

Oncogenes are mutated, amplified and/or overexpressed, altering many cellular processes to transform cells. The horizontal transfer of oncogenes to surrounding cells via EVs has been shown in several cancer models, including the oncogenic form of the epidermal growth factor receptor, EGFRvIII, in glioma (Al-Nedawi et al., 2008) and the MET oncoprotein in melanoma (Peinado et al., 2012). Mutant KRas in colorectal cancer cells alters RNA and protein sorting into small EVs and the metabolic state of recipient cells (Beckler et al., 2013; Cha et al., 2015; Hinger et al., 2018; McKenzie et al., 2016). Though several oncogenes have been shown to play a role in altering the content of EVs, a systematic analysis of how different oncogenes affect the biogenesis and release of different types of vesicles remains poorly understood.

Using an isogenic panel of oncogene-transformed epithelial cells, we examine quantitative and qualitative effects of EV release induced by different oncogenes. We find that distinct oncogenes regulate the biogenesis and release of different amounts and sizes of EVs. EVs released from transformed cells also demonstrate distinct protein and miRNA content dependent on the driver oncogenes. Thus, oncogenes regulate cellular biomass release through EVs, a new metabolic phenotype of cancer cells.

RESULTS

Oncogenes alter EV abundance and size

We sought to understand how different oncogenes alter the number and contents of EVs released from transformed cells. MCF10A cells are derived from non-tumorigenic breast tissue but are susceptible to transformation by a wide range of oncogenes, allowing us to study diverse oncogene signaling pathways (Debnath et al., 2002; Martins et al., 2015). We generated a panel of isogenic MCF10A cell lines engineered to express a variety of the most commonly mutated, amplified or overexpressed oncogenes in breast and other types of cancers (Martins et al., 2015). In order to directly compare the influence of specific oncogenic signals on EV properties we used a panel of 10 cell lines in which individual oncogenes were stably expressed (Martins et al., 2015) and compared these to cells transduced with empty vectors (i.e., Puro/Blast) (Figure 1A).

EVs were isolated using a differential ultracentrifugation method as depicted in Figure 1B (Thery et al., 2006) and processed to determine their number, size, protein and RNA content. Prior to EV collection, each cell line was cultured for 48 hours in defined medium (KSR) that does not contain exogenous EVs, normally abundant in serum-containing media. This allowed us to ensure that EVs were derived from each of the isogenic MCF10A lines. To assess the number and size of EVs produced we utilized two complementary assays. First, we performed nanoparticle tracking analysis (NTA) using conditioned media from 10 different isogenic MCF10A lines. To focus mainly on small EVs (sEVs) conditioned media was pelleted at 1000g and 2000g spins to remove cell debris, apoptotic bodies and filtered through a 0.2μ filter to remove large vesicles (lEVs) (Figure 1C–D). We found that 8 out of 9 oncogene-expressing cell lines significantly increased the number of particles released compared to control (Puro/Blast) cells (Figure 1C). Amongst the oncogenes tested, MYC and AURKB-overexpressing MCF10A cells release the greatest number of EVs compared to control cells, also significantly higher than any of the other oncogene-expressing cell lines (Figure 1C). Furthermore, the size distribution of the EVs confirmed that the majority of released vesicles are sEVs <200nm in size (Figure 1D) consistent with known size distribution for exosomes (Colombo et al., 2014). MYC and AURKB-derived EVs were smaller with a modal particle size of 116.9 nm and 119.1 nm, respectively (Figure S1A). Thus, we observed that most oncogenes induced significantly increased EV release, though MYC and AURKB vesicles were far more numerous on a per cell basis but tended to be smaller (Figure 1C–D).

NTA does not permit direct visualization of individual vesicle morphology. We therefore used transmission electron microscopy (EM) to evaluate qualitative differences and confirm size changes via direct visualization of sEVs collected from the 100K fraction (Figure 1B)

of a subset of cell lines: MYC, AURKB and HRAS(G12V) oncogene expressing and control MCF10A cells. We observed the typical cup-shaped morphology previously described for sEVs (Figure 1E) (Sahoo et al., 2011) in the 100K pellets from all of the cell lines. To elucidate the size differences of sEVs we measured the diameter of each sEV by random sampling from micrographs. The mean size of Puro/Blast sEVs is 120nm whereas the mean size of sEVs from AURKB and MYC overexpressing cells are 99nm and 96nm respectively. HRAS(G12V) sEVs were of similar size and appearance to Puro/Blast sEVs with a mean size of 122 nm. MYC and AURKB sEVs showed smaller size variance (sd ± 29, ±30nm, respectively) compared to control and HRAS(G12V) sEVs which demonstrated a wider size distribution (sd ± 52, ±42nm, respectively) (Figure 1F). These data indicate that different oncogenes alter the size but not the morphology of released sEVs. EM images also revealed the presence of some non-vesicular (NV) particles (exomere and protein aggregates) in the 100K pellet (Figure 1E), although prior fractionation studies have revealed that the majority of exomeres are retained in the supernatant of 100,000g spin (Zhang et al., 2019).

Since oncogenes induced differences in both the size and number of secreted sEVs, we asked if the total biomass of released sEVs was altered across the panel of oncogenes. Using the number of sEVs released and their size distribution from NTA, we determined the volume of cellular biomass released as sEVs and normalized to total cell number using a spherical model. We found that MYC and AURKB expressing cells released ~19.5- and ~ 14.6-fold more biomass compared to control MCF10A cells respectively (Figure 1G). We next measured cell volume to estimate percentage of cellular biomass released by EVs during a 48hr period of culture. We measured cell sizes using Countess automated cell counter and calculated cell volume using a spherical model. Control and HRAS(G12V) overexpressing MCF10A cells released less than 1% of their cellular volume whereas MYC and AURKB expressing MCF10As released 7.7% and 4.1% of their total cellular volume, respectively, via sEVs (Figure S1B). Remarkably, the volume of cells expressing either oncogene is within the same order of magnitude as control cells. Thus, MYC and AURKB overexpressing cells can significantly alter their biomass flux via sEV release compared to control MCF10A cells to maintain cellular homeostasis.

The protein content of EVs is regulated by the driver oncogene

We postulated that specific oncogenes may alter not only the size and number of sEVs released, but also their contents. To elucidate the heterogeneity of sEVs released from different oncogenes, we performed proteomic analysis of equal amounts of the 100K pellets from five different MCF10A cell lines including, control, AURKB, CCND1, HRAS(G12V), and MYC. We identified 2608 proteins with 2+ peptides using DIA profiling (Table S1). ANOVA analysis identified 319 proteins that were significantly different between the analyzed 100K fractions. PCA analysis of significantly different proteins showed that MYC and AURKB extracellular protein fractions cluster together, as do Puro/Blast and CCND1 fractions, whereas HRAS(G12V) fractions were distinct from the other groups (Figure 2A). Across all the samples we observed some shared proteins, as well as oncogene-specific proteins enriched in the 100K fractions (Figure 2B). We next sought to identify enriched biological pathways within these oncogenic EVs. KEGG pathway analysis of enriched proteins from MYC 100K fractions identified RNA transport and spliceosome function

(Figure 2C), pathways known to be upregulated by MYC in tumor cells (Hsu et al., 2015; Kress et al., 2015). The HRAS(G12V) 100K fraction was enriched with ribosome and many metabolic pathway proteins (Figure 2C). Proteins involved in metabolism and glycolysis were also identified in exosomes from mutant KRAS(G13D) colorectal cancer cells in previous studies (Beckler et al., 2013; Zhang et al., 2018b). Our observations suggest that the enrichment of metabolic pathways could be a common RAS-induced EV phenotype.

We next examined how protein markers associated with EVs differ among oncogenic EVs (Figure 2D and 2E). We included the 10K fraction in our immunoblot analysis since some of the EV markers tested are enriched in large EV (lEV) fractions. Actinin-4 is an actin-binding cytoskeleton protein identified as a lEV marker (Jeppesen et al., 2019; Kowal et al., 2016). Actinin-4 is highly abundant in HRAS(G12V)-derived lEVs (10K) (Figure 2E). Similarly, annexin-A1, which is characterized as specific lEV marker distinct from exosomes (Jeppesen et al., 2019), is enriched in the 10K fraction compared to the 100K fractions for most oncogenes, yet highly abundant in HRAS 100K fraction (Figure 2D and 2E). These results suggest that HRAS(G12V) EVs appears to be enriched with vesicles originating from plasma membranes.

Tetraspanins (i.e., CD9, CD63 and CD81) are enriched in classical exosomes but can be found in other types of EVs as well (Crescitelli et al., 2013; Kowal et al., 2016). All three tetraspanins are very abundant in AURKB and MYC fractions suggesting classical exosomes are enriched in these oncogenic fractions (Figure 2D and 2E). Alix, one of the most abundant exosomal protein, is especially highly enriched in AURKB 100K fractions (Figure 2D and 2E). Annexin-V, an apoptotic marker protein commonly identified in purified sEV fractions but absent from classical exosomes (Jeppesen et al., 2019), is significantly enriched only in the 10K and 100K fractions from HRAS(G12V) pellets (Figure 2D and 2E).

To confirm the purity of isolated EVs, we tested both the 10K and 100K fractions with known cellular markers. We tested ER marker Grp94, mitochondrial marker Cytochrome C, and a pan-histone antibody to see if our fractions were contaminated with cellular debris or apoptotic bodies. The 100K fractions were devoid of these cellular markers in all oncogenes and Grp94 and Cytochrome C was barely detected in the 10K fraction of CCND1 (Figure S2B). Moreover, we tested our fractions with markers of NV particles (exomeres) since EM images revealed some NV particles. Ago2, MVP and HSPA13 are shown to be markers of NV fractions (Jeppesen et al., 2019; Zhang et al., 2018a, 2019). HSPA13 is not detected by proteomics or western blot analysis in our 100K fractions. Low level of Ago2 is present in proteomic and western blot analysis and enriched in AURKB 100K fractions (Figure 2D and 2E). Interestingly, MVP is highly abundant in both 10K and 100K fractions and especially enriched in CCND1 preps (Figure 2D and 2E). Although MVP is suggested as NV marker (Jeppesen et al., 2019), it was found to be enriched in the 10K fraction in this study as well as in prior study (Kowal et al., 2016). Finally, we performed density gradient ultracentrifugation of the MYC 100K fractions and found that many exosome markers reside in the lighter density fraction (sEV) while markers of NV fractions such as MVP and PKM1 (glycolytic enzyme) were in the higher density fraction (NV fraction) (Figure S2D). These observations suggest that the 100K crude pellets of oncogenes contain some NV particles, but their abundance is also altered by different oncogenes. Based on these observations the

role of oncogenes in the release of NV particles and their functional roles await further investigation.

Oncogenes alter secreted miRNA composition

We next examined if secreted miRNA content depends on the oncogenic driver. We isolated equal amounts of RNA from the 100K fractions or the corresponding cells that released them. We performed qPCR analysis using a panel of 384 miRNA primers. We identified 95 miRNAs (about 1/4 of the panel) that were differentially expressed in oncogene-expressing cells compared to control cells (Figure 3A, Table S2). 72 of these miRNAs were also enriched in oncogene-derived 100K fractions compared to control 100K fractions, however there were an additional 74 miRNAs that were differentially sorted into oncogene-derived 100K fraction despite not being dysregulated in cells (Figure 3A). We performed two types of analyses on these data: 1. We asked if each oncogene caused either preferential sorting into, or exclusion from, the 100K fraction by examining the concentration of each miRNA in the 100K fraction and comparing that to the concentration of miRNAs within the cell of origin. 2. We asked if the miRNAs within the 100K fraction from each cell type differed from that of the control 100K fraction. Our goals were to discover what miRNAs the cells may be preferentially releasing, possibly to maintain homeostasis or to influence cells in their environment. We also sought to understand what miRNA handling and sorting processes may be employed when each oncogene is driving cellular phenotypes.

First, we determined which miRNAs are enriched in the 100K fraction versus their cell of origin (Figure 3B). Although the released versus cellular miRNA profiles look different for each oncogene, CCND1-overexpressing cells seem most similar to control cells in the hierarchical clustering (Figure 3B). Certain miRNAs (e.g., hsa-miR-18–3p, hsa-miR-425–3p, hsa-miR-663a) were not only enriched in several oncogene-derived fractions but also in control fractions suggesting their release is independent of oncogenic driver. On the other hand, there are certain miRNAs that are preferentially released into the 100K fraction in an oncogene-specific manner (Figure 3B).

Second, we compared miRNAs differentially released from oncogene-derived 100K fraction compared to control 100K fraction (Figure 3C, Table S3). There were 16 deregulated miRNAs common to all oncogenes either released or retained compared to control fraction (Figure 3C). AURKB and MYC derived fractions shared the highest number of deregulated miRNAs, released or retained, suggesting a common propensity to release these same miRNAs.

Third, we identified miRNAs that are uniquely over or underrepresented in 100K fractions from each oncogene-expressing cell line. CCND1 derived 100K fraction has the lowest number of differentially sorted miRNAs (3), whereas 100K fractions from AURKB, HRAS and MYC oncogene have several unique miRNAs (i.e., 24, 14, 16 respectively) (Figure 3C).

The 100K fraction-enriched miRNAs from this dataset can potentially be explored as oncogene specific markers. We selected miRNAs that are enriched in at least one of the oncogene derived fractions and presented them in Figure 3D to visualize unique or shared miRNAs (Figure 3D). miRNA-298 was the only miRNA that was upregulated in all the

oncogene-derived fractions compared to control MCF10A EV fractions. There were several miRNAs that are unique to MYC, AURKB and HRAS fractions (Figure 3D). For example, miR-95 is significantly enriched in HRAS(G12V) 100K fraction and miR-34a-5p and miR-195–5p, which are well-known tumor suppressors, is highly abundant only in the MYC 100K fraction. Our data strongly suggests that oncogenes bias which miRNAs are released and identified in the 100K fraction. This could result from oncogene specific expression of the secretion machinery, localization of the miRNA handling apparatus or miRNA binding proteins.

Thus, we asked whether the RNA motifs found within the differentially sorted miRNAs could identify oncogene-specific miRNA binding proteins. We examined known miRNA motifs shown to control sorting of miRNAs into EVs and asked if these motifs are enriched in miRNAs that are sorted into 100K fraction in an oncogene specific manner. The motif hEXO “GGYU” was found to be enriched in miRNAs sorted into hepatocyte EVs by the RNA binding protein SYNCRIP (HNRPQ) (Santangelo et al., 2016) (hereinafter hEXO SYNCRIP). Likewise, two different miRNA motifs were reported to influence sorting of miRNAs into T cell-derived EVs (Villarroya-Beltri et al., 2013). The motif “GGAG” has been shown to bind to hnRNPA2B1 and is proposed to sort miRNAs bearing this motif into EVs (hereafter hnRNPA2B1 EXO). Finally, the motif “UGCA” was found to be enriched in miRNAs *retained* in cells (hereafter CL).

We first asked if any of these motifs were found in miRNAs either preferentially released into the 100K fraction or preferentially retained in cells in common between all oncogene expressing cell lines. All three motifs were detected in half of these miRNAs (Figure 3E). The hEXO SYNCRIP binding motif was equally represented (25%) in both miRNAs enriched in EVs and those retained in cells (Figure 3E). Interestingly, hnRNPA2B1 EXO motif was observed in 16% of the miRNAs released into the 100K fractions whereas it was detected in only 4.3% of miRNAs retained in cells. In contrast, the CL motif was abundant in miRNAs retained in cells (17%) while only 6% of the miRNAs enriched in the 100K fraction contain the CL motif (Figure s3E, Table S4). Although the hEXO SYNCRIP motif was detected in more miRNAs, hnRNPA2B1 EXO motif seems to be more EV specific in MCF10A oncogene expressing cells. It is also noteworthy that half of the miRNAs either differentially secreted into the 100K fraction or retained in cells do not contain any of the previously reported sorting motifs. This suggests that miRNA secretion or cellular retention may occur via RNA binding proteins and/or mechanisms not previously described.

To further investigate oncogene-specific release, we analyzed miRNAs from MYC and HRAS derived fractions and examined the prevalence of previously identified sorting motifs. We categorized miRNAs that are common to both oncogenes, enriched in one of them compared to other, and not enriched in either (Figure 3F). miRNAs that are enriched in the 100K fraction common to both MYC and HRAS had equal representation (~25%) for both the hEXO SYNRICP and hnRNPA2B1 EXO motifs (Figure 3F). However, the hEXO SYNCRIP motif was more abundant (46%) in miRNAs that are enriched in HRAS fractions compared to MYC fractions (Figure 3F, Table S4). Interestingly, miRNAs not enriched in HRAS or MYC fractions (i.e., enriched in AURKB and/or CCDN1 fractions) are two times more likely to have the hnRNPA2B1 EXO motif (22%) compared to hEXO SYNCRIP motif

(11%). Hence, miRNAs released into HRAS derived fractions appear to contain the hEXO SYNCRIP motif more frequently than other oncogenes tested. In aggregate, mechanisms of miRNA release may be differentially employed by each cancer driver.

We also sought to determine if miRNAs enriched in the 100K fractions are associated with oncogenic or tumor suppressive functions (Table S5). For example, of the 6 miRNAs that were preferentially secreted into the 100K fractions from MYC overexpressing cells as compared to cells expressing the other oncogenes, all six have been categorized as targeting tumor suppressor or pro-growth processes ((Wang et al., 2010); Table S5). This suggests that MYC high cells eliminate growth-suppressive miRNAs via preferential EV and/or exomere release. In contrast, many of the miRNAs preferentially released from HRAS cells have been reported to have pro-tumorigenic functions (Table S5), perhaps stimulating the growth of cells within the tumor microenvironment.

Sphingolipid metabolism is altered for multiple oncogenes transformed cells but is especially critical in MYC overexpressing cells.

Due to their cone-shape structure, ceramide lipids induce negative curvature triggering inward budding of endosomal membranes (Trajkovic et al., 2008). We postulated that changes in lipid metabolism might therefore contribute to alterations in EV release by distinct oncogenes. We performed metabolomic analysis to determine how different oncogenes alter steady state abundance of lipid species in cells. We discovered significant changes in different lipids from MCF10A cells transformed by CCND1, AURKB, MYC or HRAS(G12V) relative to control MCF10A cells (Figure 4A; Table S6). Many different lipid species were highly enriched in MYC- and HRAS-overexpressing cells compared to CCND1 and AURKB overexpressing MCF10A cells (Figure 4A). Lipids with large head groups such as lysophosphatidylcholine (LPC) or phosphatidylinositol (PI) phosphates support positive curvature observed during plasma membrane budding, while phosphatidylethanolamine (PE), phosphatidic acid (PA) and diacylglycerol (DAG) which have smaller head groups, favor negative curvature (McMahon and Boucrot, 2015; Zimmerberg and Kozlov, 2006). MYC- and HRAS-overexpressing MCF10A cells were enriched with both types of lipids compared to control cells (Figure 4A). Nevertheless, ceramide lipids which induce negative curvature to generate exosomes were significantly enriched only in MYC-overexpressing MCF10A cells (Figure 4B). Ceramide can be generated via three major metabolic pathways as depicted in Figure 4C.

To evaluate lipid metabolic pathways that could contribute to EV release, we performed RNA sequencing of AURKB, MYC or HRAS(G12V) overexpressing cells which we compared to control MCF10A cells. We sought to identify deregulated enzymes in the ceramide pathway. We found that many genes involved in ceramide production were dysregulated in all three oncogenic lines. However, N-SMases, SMPD3 and SMPD4, were significantly upregulated only in MYC overexpressing cells which have the greatest abundance of ceramide lipids (Figure 4D).

These data suggest that MYC-overexpressing cells may use ceramide generation through sphingomyelin hydrolysis to produce high levels of exosomes. We tested the neutral sphingomyelinase inhibitor (GW4869) on a subset of oncogenic lines and measured EV

release through NTA. We observed a significant decrease in EV release from MYC and AURKB overexpressing cells, but not in control cells, or those expressing HRAS or CCND1 oncogenes (Figure 4E). The MYC overexpressing cells were most responsive to GW4869 treatment, suggesting that ceramide-dependent EV production is especially important in MYC high cells.

We next asked if N-SMase inhibitor treatment can alter EV protein composition from cells transformed with different oncogenes (Figure 4F). As expected, majority of EV markers exhibited significant decrease in abundance following GW4869 treatment in MYC and AURKB cells (Figure 4F, and S3). Alix was one of the most significantly downregulated protein in both AURKB and MYC 100K fraction upon GW4869 treatment, supporting the role of N-SMases in the production of syndecan-syntenin-Alix containing exosomes (Baietti et al., 2012). However, we did not see a consistent decrease in CD63 levels as observed in Syndecan-Syntenin-Alix containing exosomes(Baietti et al., 2012), suggesting that MYC and AURKB cells might produce other types of CD63-containing EVs from an alternative pathway upon N-SMase inhibition (Figure 4F, and S3).

Although HRAS(G12V) EV numbers were not changed upon GW4869 treatment (Figure 4E), we observed changes in the subtypes of released EVs in both fractions (Figure 4F, and S3). Clathrin and actinin-4 abundance were significantly decreased while Cav2- and Annexin-V-containing EVs increased in HRAS(G12V) fractions (Figure 4F, and S3). Moreover, significant changes in many markers in 10K fraction, especially lEV marker actinin-4, strengthens the observation that ceramide might also play a role in budding from the plasma membranes (Menck et al., 2017).

ESCRT pathway component *TSG101* increases EV release from AURKB and MYC overexpressing cells

The endosomal sorting complex required for transport (ESCRT) is a major regulator of MVB formation and is therefore also critical for EV release. ESCRT-0 complex recognizes and clusters ubiquitinated proteins, while ESCRT-I and -II complexes deform endosomal membranes to form buds where cargo is sorted. Finally, ESCRT-III together with accessory proteins cleave the buds to form intraluminal vesicles (ILVs) (Colombo et al., 2014; Henne et al., 2011; Wollert and Hurley, 2010) (model shown in Figure 5A). Gene expression of multiple components of the ESCRT pathway are deregulated in the context of different oncogenes compared to control cells (Figure 5B).

We sought to determine if specific oncogene expressing cells are reliant on ESCRT components for EV release. We selected two ESCRT components previously identified to be important for EV release, *TSG101* and *ALIX* (also called *PDCP6IP*) (Baietti et al., 2012; Colombo et al., 2013), and depleted their expression via siRNAs. We then performed NTA on EVs from these depleted cells (Figure 5C). We did not observe significant changes in the number of released EVs following *TSG101* knockdown from control and HRAS-overexpressing MCF10A cells. However, *TSG101* knockdown significantly decreased the number of EVs from AURKB and MYC overexpressing cells, and this decrease was most pronounced in AURKB overexpressing cells (Figure 5C). ALIX depletion was not associated with diminished EV release in any of the cell lines. Thus, TSG101, but not ALIX,

expression is important for mediating the number of EVs released from MYC and AURKB expressing cells.

We next explored if EV subtypes changed following depletion of *TSG101* or *ALIX*. As expected, most classical exosome markers decreased in the MYC and AURKB 100K fractions upon *TSG101* knockdown (Figure 5D, 5E). Although *TSG101* knockdown did not change the EV numbers from HRAS overexpressing cells (Figure 5C), the decrease in exosomal markers CD81, Alix, and syntenin-1 was compensated via increase of EV subtypes containing clathrin- and Cav2-enriched EVs (Figure 5D, 5E). Likewise, TSG101 depletion increased the Cav2- and clathrin-containing EVs in MYC fractions.

ALIX depletion did not alter the number of released EVs in any three oncogenic lines tested (Figure 5C). Still, as expected, the release of syntenin-1-containing EVs significantly decreased in all oncogenes (Baietti et al., 2012) (Figure 5D, 5E). Upon ALIX depletion, a significant increase in the subtype of CD81- and TSG101-containing EVs resulted in compensation for MYC and AURKB 100K fraction (Figure 5D, 5E). Like TSG101 depletion, ALIX depletion in HRAS cells increased the subtypes of Cav2, actinin-4, and clathrin-containing EVs (Figure 5D, 5E).

These results demonstrate that upon *TSG101* or *ALIX* depletion, oncogene-expressing MCF10A cells can induce EV release from alternative pathways (e.g.; either originating from MVBs or plasma membranes). This compensation seems to be oncogene specific. Amongst the oncogenes tested, AURKB-overexpressing cells appear to rely on ESCRT-dependent pathways more than other oncogene-overexpressing cells.

Decreased lysosomal genes and activity is associated with increased EV release

Recent studies have found that increased EV secretion can occur under conditions in which lysosome function is impaired (Adams et al., 2021; Latifkar et al., 2019; van de Vlekkert et al., 2019). Therefore, we explored if lysosomal function might be inhibited in MYC and AURKB expressing cells, the two oncogenes that account for the greatest number of released EV. Indeed, KEGG pathway analysis of RNA expression revealed that lysosomal mediated degradation is one of the most downregulated pathways for MYC and AURKB overexpressing cells, but not HRAS high cells (Figure 6A). Expression of multiple lysosome-associated enzymes are downregulated in MYC and AURKB overexpressing MCF10A cells compared to control cells (Figure 6B). The MiT/TFE family of transcriptional factors, which include TFEB, TFE3 and MITF, are key regulators of lysosome biogenesis and function (Palmieri et al., 2011; Perera and Zoncu, 2016; Sardiello et al., 2009). MiT/TFE factors are upregulated in pancreatic cancers and are required for maintaining high autophagy and lysosome activity that fuel the bioenergetic needs of tumors (Perera et al., 2015). Consistent with downregulation of a lysosome associated gene signature in MYC and AURKB cells, we find that TFE3 and TFEB are also significantly downregulated in these cells relative to control (Puro/Blast) and HRAS cells (Figure 6C). In accordance with TFEB/TFE3 downregulation, many TFEB regulated autophagy and lysosomal genes are also downregulated in AURKB and MYC cells (Figure 6D). In addition, Lysotracker dye staining, which measures lysosome pH showed a significant decrease in MYC cells, consistent with decreased lysosomal activity (Figure 6F). As

maintenance of acidic luminal pH is required for lysosomal degradation, we next determined the expression and activity of lysosome hydrolases. We found that several hydrolases including Cathepsin B (CTSB), Cathepsin D (CTSD), and Acid alpha-glycosidase (GAA) and the Mannose 6-phosphate receptor (M6PR) - a transmembrane protein essential for transport of hydrolases to the lysosome – showed significantly reduced expression in MYC and AURKB cells relative to control cells and some were increased in HRAS cells (Figure 6E). Accordingly, CTSB activity was also reduced in MYC and AURKB cells (Figure 6G), but increased in HRAS cells. Together, these data indicate that MYC and AURKB expression leads to a profound decrease in lysosome activity which, in accordance with recent studies (Adams et al., 2021; Latifkar et al., 2019; van de Vlekkert et al., 2019), favors increased EV release.

MYC overexpression increases EV production but can be attenuated by MEK/ERK signaling

In the isogenic MCF10A system MYC overexpression resulted in the greatest increase in EVs released compared to parental cells (Figure 1). MYC regulates a wide variety of processes, including but not limited to, proliferation, apoptosis and metabolism (Camarda et al., 2017; Gabay et al., 2014; Meyer and Penn, 2008) and is overexpressed in many of the most aggressive types of human cancers, such as lymphoma, receptor triple negative breast cancer, neuroblastoma and liver cancer (Horiuchi et al., 2014; Lin et al., 2012). We sought to determine if MYC overexpression affects EV production from other cell types. First, we asked if turning MYC off alters EV production. EC4 cells are derived from a conditional MYC transgenic mouse model of liver cancer in which MYC transgene expression is rapidly inhibited by treatment with doxycycline (Anderton et al., 2017; Cao et al., 2011). When MYC expression was turned off for 2 days, EV production decreased 5-fold (Figure 7A). Thus, acutely inhibiting MYC expression can rapidly reprogram cells to decrease EV release. Second, we utilized human retinal pigment epithelial (RPE) cells that constitutively overexpress human MYC (RPE-MYC) or a control plasmid (RPE-NEO) (Goga et al., 2007). MYC overexpression significantly increased EV release from RPE cells as well (~ 2-fold) (Figure 7B).

We next sought to understand how EV release is altered in human tumor cells in which MYC is known to be one of the common oncogenic drivers. First, we measured EV release from three different acute myeloid leukemia (AML) lines which have variable MYC expression (Figure 7C) and MYC copy number (Brondfield et al., 2015). We observed a strong correlation between the level of MYC overexpression and EV release in AML lines (Figure 7C, F). Next, we analyzed EV release in neuroblastoma cancer lines in which MYCN amplification is a common characteristic of aggressive neuroblastomas with the poor patient outcome (Bosse and Maris, 2016). We picked five MYCN amplified neuroblastoma lines with a range of MYCN overexpression and observed a similar trend where MYCN high cells released higher numbers of EVs (Figure 7D and 7F).

Last, we explored triple negative breast cancer cell lines, a tumor type in which MYC is frequently overexpressed (Horiuchi et al., 2012), but in which additional oncogene pathways are deregulated. For example, the SUM159 line has mutations in HRAS and PIK3CA

whereas the MDA-MB-231 line has mutations in BRAF and KRAS (Figure S4A) (Cerami et al., 2012; Gao et al., 2013). When we analyzed EV release from these five different MYC-high TNBC lines, we did not observe a correlation between MYC abundance and EV release (Figure 7E and 7F). We sought to determine if interactions with other oncogenic pathways in TNBC cells might account for this discrepancy in EV release. MDA-MB-231 cells produced the lowest number of EVs among the TNBC lines. We noticed that multiple genes involved in RAS/MEK/MAPK pathways were mutated in these cells (e.g., KRAS, BRAF, NF1) (Figure S4A). Hence, we asked if activated signaling via this pathway might diminish EV release despite the abundance of MYC expression. To test this hypothesis, we checked phosphorylated ERK, which is a downstream signal in the activated RAS/MEK/MAPK pathway (Figure 7G) and observed a significant inverse correlation between activated p-ERK levels and EV release in TNBC cells (Figure 7H). To determine if inhibition of MEK, which blocks ERK phosphorylation and activation, could elicit increased EV release in these cells, we treated MDA-MB-231 cells with the MEK inhibitor trametinib. Trametinib treatment at doses sufficient to inhibit ERK phosphorylation, resulted in a significant increase in EV release from both MDA-MB-231 and BT549 cells, without inducing an appreciable change in cell viability (Figure 7I–J and S4B). Hence, while MYC overexpression induces a cellular program that increase EV release, it can be attenuated by other signaling pathways that alters cellular homeostasis.

DISCUSSION

While oncogenes alter a variety of metabolic pathways to transform cells, we now report that they can also reprogram the size and content of released EVs and NV particles to regulate the flux of cellular biomass. In the case of MYC overexpressing cells, we find that up to 7% of cellular volume, based on a spherical volume model, may be shed via EVs every two days. MYC significantly alters ceramide metabolism by upregulating sphingomyelinases and this results in high levels of ceramides, which favor the accumulation of sEVs that originate from endosomal membranes. AURKB-overexpressing cells, in contrast, are highly dependent on the ESCRT pathway, while HRAS(G12V) expression strongly favors the release of actinin-4-, annexin-A1-, flotillin-1-, and annexin-V-containing EVs that might originate from plasma membranes. Thus, distinct oncogenes modify the number, cargo type and the likely origin of released EVs from cancer cells.

Our work found that oncogenes direct the increased release of EVs (Al-Nedawi et al., 2008; Balaj et al., 2011; Bebelman et al., 2018; Choi et al., 2017) and demonstrates that EV production depends on the driver oncogene. We find that MYC and AURKB overexpressing cells release the highest number of sEVs. MYC overexpression is associated with increased EV production in many other cell types tested; MYC-dependent increase in EV release could be a common feature of increased biomass flux and may thus represent a new metabolic parameter to consider.

Furthermore, EV populations are heterogeneous and complex. Studies performing proteomic analysis after immunoprecipitation of specific surface markers and high-resolution density gradient fractionation (Coulter et al., 2018; Jeppesen et al., 2019; Kowal et al., 2016; Zhang et al., 2018a) have revealed distinct EV subtypes. However, the field still lacks clear methods

to distinguish various sub-populations of EVs since similar sized vesicles could represent either microvesicles or exosomes. Likewise, tetraspanins could be present on vesicles of endosomal or plasma membrane origin. Additionally, both lipids and ESCRT components are involved in budding of membranes from either plasma membranes or MVBs (Mathieu et al., 2019).

Our study found that each oncogene-expressing EV population has a unique composition. MYC and AURKB EVs share similar exosome markers but *RAB5* is enriched in AURKB-derived EVs whereas clathrin-containing EVs are highly enriched in MYC-derived EVs. However, HRAS EVs are distinct form other oncogene-derived EVs and highly enriched with lEV markers like actinin-4, annexin-A1. To our knowledge, the use of isogenic cell lines is the first to describe how various oncogenes alter the heterogeneity of released EVs. Future studies should dissect the subpopulations of these EVs and NV fractions using high-density gradient fractionation and immunoisolation to define the oncogene-specific secretome further.

In addition to the heterogeneity of protein composition observed, we also found that miRNAs can be secreted or retained in cells in an oncogene-dependent manner. MYC and AURKB oncogenes share many common miRNAs enriched in the 100K fractions, whereas the miRNA content of CCND1 100K fraction is very similar to the 100K fraction released from control cells. We also identified uniquely enriched miRNAs secreted for a given oncogene which could serve as oncogene specific secretome RNA biomarkers. Both hnRNPA2B1 and SYNCRIP binding motifs are present in miRNAs secreted into oncogene derived MCF10A 100K fractions. However, these two motifs were only detected in half of the enriched miRNAs. Thus, it is likely that other RNA motifs or sorting principals may exist to regulate the sorting of other miRNAs into EVs or exomeres.

We find that specific oncogenes alter EV biogenesis pathways. MYC significantly alters ceramide lipid metabolism, a pathway that triggers the budding of endosomal membranes to produce exosomes. Inhibition of N-SMase altered the abundance of exosome markers from multiple oncogenes but diminished EV production most in MYC high cells. The ESCRT pathway is also important for EV biogenesis (Baietti et al., 2012; Colombo et al., 2013; Coulter et al., 2018). Depletion of ESCRT pathway components such as TSG101, significantly reduced EV production in AURKB and MYC cells. CD81-containing EVs were highly dependent on TSG101 in all cell types suggesting that they originate from the same ESCRT-dependent pathway. While TSG101 depletion decreased CD81-containing EVs, ALIX depletion significantly increased CD81- and TSG101-containing EV subtypes, especially in MYC and AURKB cells. TSG101 depletion significantly affects syntenin-1- and Alix-containing EVs from HRAS and MYC cells, reinforcing the role of TSG101 in the biogenesis of Syntenin-Alix-containing vesicles (Baietti et al., 2012). Interestingly, MYC cells produce clathrin-containing EVs extensively upon TSG101 depletion, whereas clathrin-containing EVs are significantly downregulated during N-SMase inhibition. Thus, MYC cells might compensate their EV pool via the ceramide pathway when TSG101 is depleted. Our results support a role for compensation between ceramide and ESCRT pathway biogenesis of EVs.

Oncogenes reprogram cellular metabolism by upregulating pathways such as glycolysis, glutaminolysis and increased lipid synthesis. These anabolic processes contribute to increases in cellular biomass which in turn permit accelerated cell division. However, to maintain cellular biomass homeostasis cells need to also degrade excess macromolecules or alternatively release them via EVs or other processes. Recent studies have demonstrated that the inhibition of lysosome function results in increased EV release (Latifkar et al., 2019; Villarroya-Beltri et al., 2016; van de Vlekkert et al., 2019) however this was not previously linked to specific oncogene function. We find that many oncogenes, but especially MYC and AURKB, can increase EV release from MCF10A cells. MYC high cells downregulate key lysosome transcription factors and lysosomal digestive enzymes required for proper lysosome function. MYC also induces an increase in ribosome biogenesis and protein synthesis (Kress et al., 2015; Ruggero, 2009). Our RNA-seq data presented in this study also shows upregulated ribosome biogenesis and protein synthesis in both in AURKB and MYC cells (GSE130768). Thus, with increased anabolic processes but with diminished lysosome activity, MYC and AURKB cells might utilize EV release to maintain their cellular homeostasis. Through increased EV release, tumor cells may thus balance anabolic processes by jettisoning unwanted macromolecules, such as tumor suppressive miRNAs, toxic lipids and other cargos. Here, we propose that understanding the principals that guide regulated release of EVs in cancer cells represents a fundamentally new way that oncogenes reprogram cellular metabolism. Differential EV release is a new metabolic phenotype which may have implications for cellular signaling, homeostasis and developmental processes.

Limitations of the Study

We acknowledge that there is an interplay between multiple oncogene pathways when they are activated together in some TNBC cells; activation of these oncogenic pathways together affects the abundance of EV release. Furthermore, we found differential oncogene-dependent miRNA release, however other types of small RNAs, not explored in this study, may also be identified as oncogene-associated RNA secretome markers. Finally, our biomass calculations were based on a spherical vesicle volume model using NTA. Further biophysical characterization of released vesicles and particles could be performed by AFM or CryoEM to assess biomass loss more precisely.

STAR METHODS

RESOURCE AVAILIBILITY

Lead Contact—Further information and requests for resources and reagents should be directed to and will be fulfilled by the lead contact, Andrei Goga (andrei.goga@ucsf.edu)

Materials availability—All unique/stable reagents (e.g., cell lines) generated in this study are available from the Lead Contact with a completed Materials Transfer Agreement, as needed.

Data and code availability—Datasets for RNA-seq have been deposited in NCBI GEO: GSE130768. Proteomics data have been deposited in ProteomeXchange under dataset identifier PXD025445, hosting repository MassIVE MSV000087219.

EXPERIMENTAL MODEL AND SUBJECT DETAILS

Cell Lines—MCF10A isogenic cell lines were stably generated using retroviral infection in our previous study (Martins et al., 2015). Control MCF10A cell line was generated using empty vectors of puromycin and blasticidin. All MCF10A cell lines were grown in DMEM/F12 containing 5% horse serum, 20ng/ml EGF, 0.5μg/ml hydrocortisone, 100ng/ml cholera toxin, 10μg/ml insulin and 1X penicillin-streptomycin (Debnath et al., 2002). The EC4 conditional liver tumor line was a gift of D. Felsher at Stanford University. EC4 cells were grown in high glucose DMEM supplemented with 10% FBS and 1X non-essential amino acids. We add 8ng/ml doxycycline to the media to turn off MYC expression (Anderton et al., 2017). RPE-NEO and RPE-MYC cells were a gift from J. Michael Bishop and cultured in DMEM supplemented with 10% FBS and 1X penicillin-streptomycin (Goga et al., 2007). AML lines were gifts from S. Kogan and cultured in RPMI containing 10% FBS. Neuroblastoma lines were gift of W. A. Weiss and maintained in RPMI containing 10% FBS and 2mM L-glutamine. The culture conditions for TNBC lines have been previously described (Neve et al., 2006). Briefly, MDA-MB-231 cells were grown in DMEM supplemented with 10% FBS and 1X penicillin-streptomycin. HCC1143, BT549, breast cancer cell lines were grown in RPMI supplemented with 10% FBS and 1X penicillin-streptomycin. SUM149 and SUM159 lines were grown in Ham's F12 supplemented with 5%FBS, 10μg/ml insulin, 0.5μg/ml hydrocortisone, and 1X penicillin-streptomycin.

METHOD DETAILS

Nanoparticle Tracking Analysis (NTA)—We seeded 2×10^5 cells / well into 6 well dishes and replaced media with 5% KSR (Knockout Serum Replacement) (Gibco) containing media the next day. We cultured cells in 5% KSR media for 48 hours. The conditioned media was collected and centrifuged at 1000g spin for 10 mins. Then supernatant was centrifuged at 2000g for 20mins. The supernatant from 2000g spin was filtered through a 0.2μ filter. We performed nanoparticle tracking analysis (NTA) using NanoSight LM10 or Nanosight NS300 (Malvern Panalytical). We kept all the settings (gain, camera level, and thresholds) for capturing the videos and analysis constant for all samples. We measured each sample 3 times for 30s. We used Nanoparticle Tracking Analysis Software 3.2. For each sample, cells were collected, stained with Trypan Blue Stain (0.4%) (Invitrogen) and counted using Countess Automated Cell Counter (Invitrogen) according to the manufacturer's instructions to determine viable cell number. We used cells with more than %90–95 viability. We normalized particle count to the cell number.

EV isolation—The equal number of cells were seeded, and next day media was replaced with 5% KSR (Knockout Serum Replacement) after washing twice with PBS. EVs were isolated using differential centrifugation after 48 hours of media change (Figure 1B). Briefly, the condition media collected and centrifuged at 1000g for 10 mins at 4°C to pellet cells. Supernatant was centrifuged at 2000g for 20min at 4°C, then supernatant transferred to the new tubes and centrifuged at 10,000g for 30 min at 4°C (pellet of this spin was 10K fraction). The supernatant filtered through 0.22μ filter and transferred to a Beckman tube and centrifuged at 100,000g for 2 hours using SW28 rotor (Beckman). Supernatant was removed leaving 1ml behind. The remaining 1ml supernatant was then mixed with pellet and transferred to a Beckman Eppendorf tube and re-centrifuged at 100,000g using rotor

TLA-100.3 (pellet of this spin is 100K fraction). Cells from the first 1000g pellet were pooled with cells trypsinized from the plates and counted by Countess (Invitrogen) using Trypan Blue stain 0.4% (Invitrogen). The cells with more than >90% cell viability is used in the analysis. EVs were isolated from three 10cm plates for determining the protein composition of EVs (Figure 2E). For GW4869 and siRNA knockdowns, one 10cm plate was used for EV isolation (Figure 4 and 5).

5%−40% iodixanol density gradient fractionation—Cushioned density gradient ultracentrifugation was performed as described previously (Li et al., 2018). Briefly, condition media spun at 1000g, 2000g and 10,000g then filtered through a 0.2μ filter to remove cell debris, apoptotic bodies and lEVs. Next, 34ml condition media was transferred to ultracentrifuge tube, underlaid with 2ml 60% iodixanol (Sigma) and spun at 100,000g for 2 hours. Bottom 3ml volume is collected and mixed to create 40% iodixanol. 5%, 10%, 20% iodixanol gradients were prepared using homogenization buffer. Starting from 5% gradient each layer underlaid to the bottom of the tube and finally 40% gradient placed to the bottom creating discontinuous gradient. Tubes were subjected to ultracentrifugation at 100,000g for 18 hours at 4°C. Twelve 1ml fractions are collected from the top of the gradient.

Electron Microscopy—~5–6μl of the resuspended 100,000 ×g pellet fraction was spread onto glow discharged Formvar-coated copper mesh grids (Electron Microscopy Sciences) and stained with 2% Uranyl acetate for 2 min. Excess staining solution was blotted off with filter paper. After drying, grids were imaged at at 120 kV using a Tecnai 12 Transmission Electron Microscope (FEI, Hillsboro, OR). EV size analysis on micrographs were done using Fiji software.

EV and cell volume calculations—We assumed released EVs as spherical particles and performed a biomass calculation as follows: 1) we calculated the volume of the sphere (vesicle) by each size range, 2) we multiplied the frequency (number) of the vesicles by each size range, 3) we summed all size ranges to get a total volume of the released biomass, 4) we divided total volume by cell number for normalization.

We measured cell size using Countess automated cell counter (Invitrogen). We measured each cell line at least four times and take average of measured cell sizes. We assumed cells as spheres and calculated their volume.

Proteomics

Protein digestion: Protein concentration was determined by BCA assay and (Pierce), 50ug of EVs was digested on a S-trap Micro spin digestion column. Initially, 10 mM dithiothreitol (DTT) was added and incubated at 50°C for 10 min and rested at room temperature for 10 min. Next, 5 mM iodoacetamide (IAA) was added and incubated at room temperature for 30 min in the dark. The samples were acidified with 12% phosphoric acid followed by the addition of 2.348 mL of freshly made S-trap buffer (90% methanol, 100 mM TEAB, pH 7.1) and mixed immediately by inversion. The entire acidified lysate/St-buffer mix was transferred to the S-trap spin column and centrifuged at 3,000 rcf for 1 min or until all the solution passed through the column. Columns were washed with 400 uL of S-trap buffer and

centrifuged at 4,000 rcf until dry. Columns were transferred to a clean elution tube. Trypsin enzyme digest buffer was carefully added (1:25 enzyme: total protein in 121 uL 50mM TEAB, pH 8.0) to the column and followed by incubation at 37°C overnight. After the first hour, the trypsin digestion step was repeated. Peptide elution steps included 80 uL of 50 mM TEAB (pH 8.0) followed by centrifugation at 1,000 rcf for 1 min, 80 uL of 0.5% formic acid followed by centrifugation at 1,000 rcf for 1 min, 80 uL of the solution containing 50% acetonitrile and 0.5% formic acid followed by centrifugation at 4,000 rcf for 1 min. The final pooled elution was dried down in a speed-vacuum. Peptides were resuspended in 0.1% TFA 2% ACN and quantified using Pierce™ Quantitative Fluorometric Peptide Assay (Thermo Fisher Scientific). Equal portions of all samples were mixed together to make a reference sample to be run multiple times for chromatogram library runs.

Liquid chromatography tandem mass spectrometry : The next steps were processed at the UC Davis Proteomics Core Facility. Peptides were trapped on a Thermo PepMap trap and separated on an Easy-spray 100 um x 25 cm C18 column using a Dionex Ultimate 3000 nUPLC at 200 nl/min. Solvent A= 0.1% formic acid, Solvent B = 100% Acetonitrile 0.1% formic acid. Gradient conditions = 2%B to 50%B over 60 minutes, followed by a 50%−99% B in 6 minutes and then held for 3 minutes than 99%B to 2%B in 2 minutes and total run time of 90 minutes using Thermo Scientific Fusion Lumos mass spectrometer running in Data Independent Acquisition (DIA) mode. Each individual sample was run using a 2x gas phase fractionation strategy where each sample was analyzed two times with the first gas phase fraction being between 360–760 m/z, the second being 760–1158 m/z. Both gas phase fractions used 4 Da non-overlapping windows.

Data analysis and raw data processing : Data analyzed using Scaffold DIA v.2.0.0 (Proteome Software, Portland, OR, USA). Raw data files were converted to mzML format using ProteoWizard (Chambers et al., 2012). Each raw data file was searched against the Pan human SWATH Library (Rosenberger et al., 2014). Variable modifications considered were oxidation of methionine and static modifications were carbamidomethyl of cysteine. The digestion enzyme was assumed to be Trypsin with a maximum of 1 missed cleavage site(s) allowed. Only peptides with charges in the range [2..3] and length in the range [6..30] were considered. Peptides identified in each search were filtered by Percolator (3.01.nightly-13–655e4c7-dirty) (Kall et al., 2008; Käll et al., 2007, 2008) to achieve a maximum FDR of 0.01. Individual search results were combined, and peptides were again filtered to an FDR threshold of 0.01 for inclusion in the reference library.

Quantification and criteria for protein identification: Peptide quantification was performed by EncyclopeDIA v. 0.9.2. For each peptide, the five highest quality fragment ions were selected for quantitation. Proteins that contained similar peptides and could not be differentiated based on MS/MS analysis were grouped to satisfy the principles of parsimony. Only proteins with a minimum of two identified peptides were considered and filtered by a protein FDR threshold of 1.0%.

Western Blot Analysis—Cells, 10K and 100K pellets were lysed in Pierce RIPA buffer (25mM Tris-HCl (pH 7.6), 150mM NaCl, 1% NP-40, 1% sodium deoxycholate, 0.1% SDS)

supplemented with protease and phosphatase inhibitor cocktail (Roche) on ice for 20 mins. Lysates were spun down at 13,000g for 15 mins at 4°C. Protein concentration was determined using the DC Protein Assay (BioRad). For whole cell lysates, 30 μg protein extracts were resolved using 4–12% SDS-PAGE gels (Life Technologies) and transferred to nitrocellulose membranes using iBlot (Life Technologies). For 10K and 100K fractions, the equal number of cells were seeded at the beginning of each experiment, and EV pellets were resuspended in the same volume of RIPA buffer and same volume loaded for SDS-PAGE. Membranes were probed with primary antibodies overnight on a 4°C shaker, then incubated with horseradish peroxidase (HRP)-conjugated secondary antibodies, and signals were visualized with Visualizer™ Western Blot Detection Kit (Millipore). Band analysis was performed using ImageLab software from BioRAD and intensities are normalized to cell counts.

RNA isolation and qPCR—RNA from cells and EVs was isolated using mirRNeasy micro kit (Qiagen). cDNA was prepared using Universal cDNA synthesis kit according to manufacturer's instructions (Exiqon/Qiagen). qPCR was performed using miRCURY LNA miRNA Human Panel I according to manufacturer's instructions (Exiqon/Qiagen). The data was analyzed using GenEX software (MultiD) according to manufacturer's instructions. Normalization was performed using NormFinder tool of the software. Three independent replicates were used for MYC and Puro/Blast cell and EV samples. Two independent replicates were processed for HRAS, CCND1, AURKB cell and EV samples.

RNA sequencing—RNA was isolated using RNeasy mini kit according to manufacturer's instructions (Qiagen). Three different samples of RNA were isolated for each MCF10A line (i.e., Puro/Blast, MYC, AURKB and HRAS). Library preparation and Illumina sequencing were performed at Novogene Corporation (Sacramento, CA) (en.novogene.org). Briefly, mRNA from Eukaryote organisms was purified from total RNA using poly-T oligo-attached magnetic beads. The mRNA was first fragmented randomly by addition of fragmentation buffer, then NEB library was prepared. Q-PCR is used to accurately quantify the library effective concentration (> 2nM), in order to ensure the library quality. Libraries fed into Illumina Platform, and paired-end reads were generated. Downstream analysis was performed using a combination of programs including STAR, HTseq, Cufflink and Novogene's wrapped scripts. Alignments were parsed using Tophat program and differential expressions were determined through DESeq2/edgeR. Heat maps were generated with the gplots package in R (version 3.3.1).

Metabolomic profiling—Metabolomic analyses were conducted as previously described in Louie et. al. (Louie et al., 2016). Briefly, 2 million cells were plated overnight, serum starved for 2 hours prior to harvesting, after which cells were washed twice with PBS, harvested by scraping, and flash frozen. For nonpolar metabolomic analyses, flash frozen cell pellets were extracted in 4mL of 2:1:1 chloroform/methanol/PBS with internal standards dodecylglycerol (10 nmoles) and pentadecanoic acid (10 nmoles). Organic and aqueous layers were separated by centrifugation, and organic layer was extracted. Aqueous layer was acidified with 0.1% formic acid followed by re-extraction with 2 mL chloroform. The second organic layer was combined with the first extract and dried under nitrogen, after

which lipids were resuspended in chloroform (120 μl). A 10 μl aliquot was then analyzed by both single-reaction monitoring (SRM)-based LC-MS/MS or untargeted LC-MS. For polar metabolomic analyses, frozen cell pellets were extracted in 180 μl of 40:40:20 acetonitrile/methanol/water with internal standard d3 N15- serine (1 nmole). Following vortexing and bath sonication, the polar metabolite fraction (supernatant) was isolated by centrifugation. A 20 μl aliquot was then analyzed by both single-reaction monitoring (SRM)-based LC-MS/MS or untargeted LC-MS. Relative levels of metabolites were quantified by integrating the area under the curve for each metabolite, normalizing to internal standard values, and then normalizing to the average values of the control groups.

GW4869 treatment—1×10^5 cells seeded into one well of 6well plates at the beginning of experiment. The media changed to 5% KSR with 5μM GW4869 (Sigma) or vehicle, DMSO (Sigma) on the next day. Condition media collected after 48 hours and NTA was performed as described above. For western blot experiments, 7.5×10^5 cells were seeded into one 10cm dish.

RNAi knockdown—*TSG101*-specific (L-003549–00-0005), *ALIX*-specific (L-004233–00-0005) and nontargeting (D-001810–10-20) siRNAs were purchased from GE Dharmacon (SMARTpool, four siRNAs per gene). 30 pmol siRNA was used to transfect cells with the Lipofectamine RNAiMAX Transfection Reagent (Life Technologies), according to the manufacturer's instructions. Cells were incubated with siRNA and at 24 hrs media was changed to 5%KSR. Cells were incubated for additional 48hrs to collect EVs. At the beginning of experiments, 1×10^5 cells seeded per well of 6-well plates for NTA analysis and 7.5×10^5 cells per 10cm dish for western blot analysis. At the end point, cells were collected, stained with Trypan Blue Stain (0.4%) (Invitrogen) and counted using Countess Automated Cell Counter (Invitrogen) according to the manufacturer's instructions. Particle counts and band intensities are normalized to the cell number.

Immunofluorescence—MCF10A (200K cells per condition) were seeded on fibronectin coated coverslips in 12 well plate. Lysotracker Red-DND-99 was purchased from Thermo scientific and used at 100nM in a 5% CO2 atmosphere at 37 °C for 30 min. Stock solutions of Magic Red were prepared in DMSO and added to cells for 60 mins at 37°C. Following incubation, media was removed, and cells were rinsed with PBS and fixed with 4% PFA for 15mins. After fixing, cells were washed twice with PBS and mounted with DAPI fluoromount G and imaged on a Zeiss Laser Scanning Microscope (LSM) 710 using a 63x objective. Mean fluorescence intensity was measured using ImageJ software from 10–30 independent fields by subtracting the mean fluorescence of the background. Mean of Puro/Blast samples was used for normalization.

QUANTIFICATION AND STATISTICAL ANALYSIS

Statistical analyses were performed using GraphPad Prism 9 software. Groups were compared using unpaired or paired Student's t-test. Pearson correlations were calculated using Prism 9. One way ANOVA followed by multiple test correction (control FDR with standard Benjamini-Hochberg procedure) was performed using Scaffold DIA software for proteomics data. R package was used to create heatmaps. Details regarding the statistical

analysis of the data are provided in the corresponding figure legends and/or the Methods sections above. p values of less than 0.05 are considered to be significant.

Supplementary Material

Refer to Web version on PubMed Central for supplementary material.

ACKNOWLEDGMENTS

This publication is part of the NIH Extracellular RNA Communication Consortium paper package and was supported by the NIH Common Fund's exRNA Communication Program. We thank Andrew Leidal, Jayanta Debnath, Scott Kogan, and Catherine Smith for equipment, cell line and reagent sharing. We thank all the members of Goga lab for their help and support. We thank the staff at the UC Berkeley Electron Microscope Laboratory for advice and assistance in EM sample preparation and data collection. We also thank UC Davis Proteomic Core for their help with proteomic analysis. LC-MS was supported by a NIH shared instrumentation grant S10OD021801. We acknowledge the PFCC (RRID:*SCR_018206*) for providing access to Nanosight NS300 (NIH P30 DK063720). The work was funded by NIH (1U19CA179512 to A.G. and N.D.L.) and (R01CA223817 to A.G.), the NIH F99/K00 Award (F99CA212488 to R.C.), the CDMRP (W81XWH-18-1-0713) and the Mark Foundation. S.K. is supported by the NIH NCI 2T32CA108462. R.M.P is the Nadia's Gift Foundation Innovator of the Damon Runyon Cancer Research Foundation (DRR-46-17) and is supported by NIH (1DP2CA216364) and Pancreatic Cancer Action Network Career Development Award.

REFERENCES

Adams SD, Csere J, D'angelo G, Carter EP, Romao M, Arnandis T, Dodel M, Kocher HM, Grose R, Raposo G, et al. (2021). Centrosome amplification mediates small extracellular vesicle secretion via lysosome disruption. Current Biology S0960982221000610.

Al-Nedawi K, Meehan B, Micallef J, Lhotak V, May L, Guha A, and Rak J (2008). Intercellular transfer of the oncogenic receptor EGFRvIII by microvesicles derived from tumour cells. Nat Cell Biol 10, 619–624. [PubMed: 18425114]

Andaloussi SE, Mager I, Breakefield XO, and Wood MJ (2013). Extracellular vesicles: biology and emerging therapeutic opportunities. Nature Reviews.Drug Discovery 12, 347–357. [PubMed: 23584393]

Anderton B, Camarda R, Balakrishnan S, Balakrishnan A, Kohnz RA, Lim L, Evason KJ, Momcilovic O, Kruttwig K, Huang Q, et al. (2017). MYC-driven inhibition of the glutamate-cysteine ligase promotes glutathione depletion in liver cancer. EMBO Reports 18, 569–585. [PubMed: 28219903]

Baietti MF, Zhang Z, Mortier E, Melchior A, Degeest G, Geeraerts A, Ivarsson Y, Depoortere F, Coomans C, Vermeiren E, et al. (2012). Syndecan-syntenin-ALIX regulates the biogenesis of exosomes. Nature Cell Biology 14, 677–685. [PubMed: 22660413]

Balaj L, Lessard R, Dai L, Cho YJ, Pomeroy SL, Breakefield XO, and Skog J (2011). Tumour microvesicles contain retrotransposon elements and amplified oncogene sequences. Nature Communications 2, 180.

Bebelman MP, Smit MJ, Pegtel DM, and Baglio SR (2018). Biogenesis and function of extracellular vesicles in cancer. Pharmacology & Therapeutics 188, 1–11. [PubMed: 29476772]

Becker A, Thakur BK, Weiss JM, Kim HS, Peinado H, and Lyden D (2016). Extracellular Vesicles in Cancer: Cell-to-Cell Mediators of Metastasis. Cancer Cell 30, 836–848. [PubMed: 27960084]

Beckler MD, Higginbotham JN, Franklin JL, Ham AJ, Halvey PJ, Imasuen IE, Whitwell C, Li M, Liebler DC, and Coffey RJ (2013). Proteomic analysis of exosomes from mutant KRAS colon cancer cells identifies intercellular transfer of mutant KRAS. Molecular & Cellular Proteomics : MCP 12, 343–355. [PubMed: 23161513]

Bosse KR, and Maris JM (2016). Advances in the translational genomics of neuroblastoma: From improving risk stratification and revealing novel biology to identifying actionable genomic alterations: Advances in Neuroblastoma Genomics. Cancer 122, 20–33. [PubMed: 26539795]

Brondfield S, Umesh S, Corella A, Zuber J, Rappaport AR, Gaillard C, Lowe SW, Goga A, and Kogan SC (2015). Direct and indirect targeting of MYC to treat acute myeloid leukemia. Cancer Chemother Pharmacol 76, 35–46. [PubMed: 25956709]

Camarda R, Zhou AY, Kohnz RA, Balakrishnan S, Mahieu C, Anderton B, Eyob H, Kajimura S, Tward A, Krings G, et al. (2016). Inhibition of fatty acid oxidation as a therapy for MYC-overexpressing triple-negative breast cancer. Nat Med 22, 427–432. [PubMed: 26950360]

Camarda R, Williams J, and Goga A (2017). In vivo Reprogramming of Cancer Metabolism by MYC. Frontiers in Cell and Developmental Biology 5, 35. [PubMed: 28443280]

Cao Z, Fan-Minogue H, Bellovin DI, Yevtodiyenko A, Arzeno J, Yang Q, Gambhir SS, and Felsher DW (2011). MYC phosphorylation, activation, and tumorigenic potential in hepatocellular carcinoma are regulated by HMG-CoA reductase. Cancer Research 71, 2286–2297. [PubMed: 21262914]

Cerami E, Gao J, Dogrusoz U, Gross BE, Sumer SO, Aksoy BA, Jacobsen A, Byrne CJ, Heuer ML, Larsson E, et al. (2012). The cBio Cancer Genomics Portal: An Open Platform for Exploring Multidimensional Cancer Genomics Data: Figure 1. Cancer Discovery 2, 401–404. [PubMed: 22588877]

Cha DJ, Franklin JL, Dou Y, Liu Q, Higginbotham JN, Beckler MD, Weaver AM, Vickers K, Prasad N, Levy S, et al. (2015). KRAS-dependent sorting of miRNA to exosomes. ELife 4, e07197. [PubMed: 26132860]

Chambers MC, Maclean B, Burke R, Amodei D, Ruderman DL, Neumann S, Gatto L, Fischer B, Pratt B, Egertson J, et al. (2012). A cross-platform toolkit for mass spectrometry and proteomics. Nat Biotechnol 30, 918–920. [PubMed: 23051804]

Choi D, Lee TH, Spinelli C, Chennakrishnaiah S, D'Asti E, and Rak J (2017). Extracellular vesicle communication pathways as regulatory targets of oncogenic transformation. Seminars in Cell & Developmental Biology 67, 11–22. [PubMed: 28077296]

Colombo M, Moita C, Niel G. van, Kowal J, Vigneron J, Benaroch P, Manel N, Moita LF, Thery C, and Raposo G (2013). Analysis of ESCRT functions in exosome biogenesis, composition and secretion highlights the heterogeneity of extracellular vesicles. Journal of Cell Science 126, 5553–5565. [PubMed: 24105262]

Colombo M, Raposo G, and Théry C (2014). Biogenesis, Secretion, and Intercellular Interactions of Exosomes and Other Extracellular Vesicles. Annu. Rev. Cell Dev. Biol. 30, 255–289. [PubMed: 25288114]

Commisso C, Davidson SM, Soydaner-Azeloglu RG, Parker SJ, Kamphorst JJ, Hackett S, Grabocka E, Nofal M, Drebin JA, Thompson CB, et al. (2013). Macropinocytosis of protein is an amino acid supply route in Ras-transformed cells. Nature 497, 633–637. [PubMed: 23665962]

Coulter ME, Dorobantu CM, Lodewijk GA, Delalande F, Cianferani S, Ganesh VS, Smith RS, Lim ET, Xu CS, Pang S, et al. (2018). The ESCRT-III Protein CHMP1A Mediates Secretion of Sonic Hedgehog on a Distinctive Subtype of Extracellular Vesicles. Cell Reports 24, 973–986.e8. [PubMed: 30044992]

Crescitelli R, Lasser C, Szabo TG, Kittel A, Eldh M, Dianzani I, Buzas EI, and Lotvall J (2013). Distinct RNA profiles in subpopulations of extracellular vesicles: apoptotic bodies, microvesicles and exosomes. Journal of Extracellular Vesicles 2, 10.3402/jev.v2i0.20677. eCollection 2013.

DeBerardinis RJ, and Chandel NS (2016). Fundamentals of cancer metabolism. Sci. Adv 2, e1600200. [PubMed: 27386546]

DeBerardinis RJ, Lum JJ, Hatzivassiliou G, and Thompson CB (2008). The biology of cancer: metabolic reprogramming fuels cell growth and proliferation. Cell Metabolism 7, 11–20. [PubMed: 18177721]

Debnath J, Mills KR, Collins NL, Reginato MJ, Muthuswamy SK, and Brugge JS (2002). The role of apoptosis in creating and maintaining luminal space within normal and oncogene-expressing mammary acini. Cell 111, 29–40. [PubMed: 12372298]

Desrochers LM, Antonyak MA, and Cerione RA (2016). Extracellular Vesicles: Satellites of Information Transfer in Cancer and Stem Cell Biology. Developmental Cell 37, 301–309. [PubMed: 27219060]

Gabay M, Li Y, and Felsher DW (2014). MYC activation is a hallmark of cancer initiation and maintenance. Cold Spring Harbor Perspectives in Medicine 4, 10.1101/cshperspect.a014241.

Galluzzi L, Pietrocola F, Levine B, and Kroemer G (2014). Metabolic Control of Autophagy. Cell 159, 1263–1276. [PubMed: 25480292]

Gao J, Aksoy BA, Dogrusoz U, Dresdner G, Gross B, Sumer SO, Sun Y, Jacobsen A, Sinha R, Larsson E, et al. (2013). Integrative Analysis of Complex Cancer Genomics and Clinical Profiles Using the cBioPortal. Science Signaling 6, pl1–pl1. [PubMed: 23550210]

Goga A, Yang D, Tward AD, Morgan DO, and Bishop JM (2007). Inhibition of CDK1 as a potential therapy for tumors over-expressing MYC. Nat Med 13, 820–827. [PubMed: 17589519]

Guo JY, Chen HY, Mathew R, Fan J, Strohecker AM, Karsli-Uzunbas G, Kamphorst JJ, Chen G, Lemons JM, Karantza V, et al. (2011). Activated Ras requires autophagy to maintain oxidative metabolism and tumorigenesis. Genes & Development 25, 460–470.

Gustafson D, Veitch S, and Fish JE (2017). Extracellular Vesicles as Protagonists of Diabetic Cardiovascular Pathology. Frontiers in Cardiovascular Medicine 4, 71. [PubMed: 29209616]

Henne WM, Buchkovich NJ, and Emr SD (2011). The ESCRT pathway. Developmental Cell 21, 77–91. [PubMed: 21763610]

Hinger SA, Cha DJ, Franklin JL, Higginbotham JN, Dou Y, Ping J, Shu L, Prasad N, Levy S, Zhang B, et al. (2018). Diverse Long RNAs Are Differentially Sorted into Extracellular Vesicles Secreted by Colorectal Cancer Cells. Cell Reports 25, 715–725.e4. [PubMed: 30332650]

Horiuchi D, Kusdra L, Huskey NE, Chandriani S, Lenburg ME, Gonzalez-Angulo AM, Creasman KJ, Bazarov AV, Smyth JW, Davis SE, et al. (2012). MYC pathway activation in triple-negative breast cancer is synthetic lethal with CDK inhibition. The Journal of Experimental Medicine 209, 679–696. [PubMed: 22430491]

Horiuchi D, Anderton B, and Goga A (2014). Taking on challenging targets: making MYC druggable. American Society of Clinical Oncology Educational Book.American Society of Clinical Oncology.Annual Meeting 497.

Hsu TY-T, Simon LM, Neill NJ, Marcotte R, Sayad A, Bland CS, Echeverria GV, Sun T, Kurley SJ, Tyagi S, et al. (2015). The spliceosome is a therapeutic vulnerability in MYC-driven cancer. Nature 525, 384–388. [PubMed: 26331541]

Jeppesen DK, Fenix AM, Franklin JL, Higginbotham JN, Zhang Q, Zimmerman LJ, Liebler DC, Ping J, Liu Q, Evans R, et al. (2019). Reassessment of Exosome Composition. Cell 177, 428–445.e18. [PubMed: 30951670]

Käll L, Canterbury JD, Weston J, Noble WS, and MacCoss MJ (2007). Semi-supervised learning for peptide identification from shotgun proteomics datasets. Nat Methods 4, 923–925. [PubMed: 17952086]

Kall L, Storey JD, and Noble WS (2008). Non-parametric estimation of posterior error probabilities associated with peptides identified by tandem mass spectrometry. Bioinformatics 24, i42–i48. [PubMed: 18689838]

Käll L, Storey JD, MacCoss MJ, and Noble WS (2008). Assigning Significance to Peptides Identified by Tandem Mass Spectrometry Using Decoy Databases. J. Proteome Res. 7, 29–34. [PubMed: 18067246]

Kalluri R (2016). The biology and function of exosomes in cancer. Journal of Clinical Investigation 126, 1208–1215.

Kanlikilicer P, Rashed MH, Bayraktar R, Mitra R, Ivan C, Aslan B, Zhang X, Filant J, Silva AM, Rodriguez-Aguayo C, et al. (2016). Ubiquitous Release of Exosomal Tumor Suppressor miR-6126 from Ovarian Cancer Cells. Cancer Research 76, 7194–7207. [PubMed: 27742688]

Kitatani K, Idkowiak-Baldys J, and Hannun YA (2008). The sphingolipid salvage pathway in ceramide metabolism and signaling. Cellular Signalling 20, 1010–1018. [PubMed: 18191382]

Kowal J, Arras G, Colombo M, Jouve M, Morath JP, Primdal-Bengtson B, Dingli F, Loew D, Tkach M, and Thery C (2016). Proteomic comparison defines novel markers to characterize heterogeneous populations of extracellular vesicle subtypes. Proceedings of the National Academy of Sciences of the United States of America 113, 968.

Kress TR, Sabò A, and Amati B (2015). MYC: connecting selective transcriptional control to global RNA production. Nat Rev Cancer 15, 593–607. [PubMed: 26383138]

Latifkar A, Ling L, Hingorani A, Johansen E, Clement A, Zhang X, Hartman J, Fischbach C, Lin H, Cerione RA, et al. (2019). Loss of Sirtuin 1 Alters the Secretome of Breast Cancer Cells by Impairing Lysosomal Integrity. Developmental Cell 49, 393–408.e7. [PubMed: 30982660]

Li K, Wong DK, Hong KY, and Raffai RL (2018). Cushioned–Density Gradient Ultracentrifugation (C-DGUC): A Refined and High Performance Method for the Isolation, Characterization, and Use of Exosomes. In Extracellular RNA, Patel T, ed. (New York, NY: Springer New York), pp. 69–83.

Lin CY, Loven J, Rahl PB, Paranal RM, Burge CB, Bradner JE, Lee TI, and Young RA (2012). Transcriptional amplification in tumor cells with elevated c-Myc. Cell 151, 56–67. [PubMed: 23021215]

Luga V, Zhang L, Viloria-Petit AM, Ogunjimi AA, Inanlou MR, Chiu E, Buchanan M, Hosein AN, Basik M, and Wrana JL (2012). Exosomes mediate stromal mobilization of autocrine Wnt-PCP signaling in breast cancer cell migration. Cell 151, 1542–1556. [PubMed: 23260141]

Martins MM, Zhou AY, Corella A, Horiuchi D, Yau C, Rakhshandehroo T, Gordan JD, Levin RS, Johnson J, Jascur J, et al. (2015). Linking Tumor Mutations to Drug Responses via a Quantitative Chemical–Genetic Interaction Map. Cancer Discovery 5, 154–167. [PubMed: 25501949]

Mathieu M, Martin-Jaular L, Lavieu G, and Thery C (2019). Specificities of secretion and uptake of exosomes and other extracellular vesicles for cell-to-cell communication. Nature Cell Biology 21, 9–17. [PubMed: 30602770]

McKenzie AJ, Hoshino D, Hong NH, Cha DJ, Franklin JL, Coffey RJ, Patton JG, and Weaver AM (2016). KRAS-MEK Signaling Controls Ago2 Sorting into Exosomes. Cell Reports 15, 978–987. [PubMed: 27117408]

McMahon HT, and Boucrot E (2015). Membrane curvature at a glance. Journal of Cell Science 128, 1065–1070. [PubMed: 25774051]

Menck K, Sonmezer C, Worst TS, Schulz M, Dihazi GH, Streit F, Erdmann G, Kling S, Boutros M, Binder C, et al. (2017). Neutral sphingomyelinases control extracellular vesicles budding from the plasma membrane. Journal of Extracellular Vesicles 6, 1378056. [PubMed: 29184623]

Meyer N, and Penn LZ (2008). Reflecting on 25 years with MYC. Nature Reviews.Cancer 8, 976–990. [PubMed: 19029958]

Minciacchi VR, Freeman MR, and Di Vizio D (2015). Extracellular Vesicles in Cancer: Exosomes, Microvesicles and the Emerging Role of Large Oncosomes. Seminars in Cell & Developmental Biology 40, 41–51. [PubMed: 25721812]

Minciacchi VR, Spinelli C, Reis-Sobreiro M, Cavallini L, You S, Zandian M, Li X, Mishra R, Chiarugi P, Adam RM, et al. (2017). MYC Mediates Large Oncosome-Induced Fibroblast Reprogramming in Prostate Cancer. Cancer Research 77, 2306–2317. [PubMed: 28202510]

Nabet BY, Qiu Y, Shabason JE, Wu TJ, Yoon T, Kim BC, Benci JL, DeMichele AM, Tchou J, Marcotrigiano J, et al. (2017). Exosome RNA Unshielding Couples Stromal Activation to Pattern Recognition Receptor Signaling in Cancer. Cell 170, 352–366.e13. [PubMed: 28709002]

Neve RM, Chin K, Fridlyand J, Yeh J, Baehner FL, Fevr T, Clark L, Bayani N, Coppe J-P, Tong F, et al. (2006). A collection of breast cancer cell lines for the study of functionally distinct cancer subtypes. Cancer Cell 10, 515–527. [PubMed: 17157791]

Palmieri M, Impey S, Kang H, di Ronza A, Pelz C, Sardiello M, and Ballabio A (2011). Characterization of the CLEAR network reveals an integrated control of cellular clearance pathways. Human Molecular Genetics 20, 3852–3866. [PubMed: 21752829]

Peinado H, Alečković M, Lavotshkin S, Matei I, Costa-Silva B, Moreno-Bueno G, Hergueta-Redondo M, Williams C, García-Santos G, Ghajar CM, et al. (2012). Melanoma exosomes educate bone marrow progenitor cells toward a pro-metastatic phenotype through MET. Nat Med 18, 883–891. [PubMed: 22635005]

Perera RM, and Zoncu R (2016). The Lysosome as a Regulatory Hub. Annual Review of Cell and Developmental Biology 32, 223–253.

Perera RM, Stoykova S, Nicolay BN, Ross KN, Fitamant J, Boukhali M, Lengrand J, Deshpande V, Selig MK, Ferrone CR, et al. (2015). Transcriptional control of autophagy-lysosome function drives pancreatic cancer metabolism. Nature 524, 361–365. [PubMed: 26168401]

Poggio M, Hu T, Pai C-C, Chu B, Belair CD, Chang A, Montabana E, Lang UE, Fu Q, Fong L, et al. (2019). Suppression of Exosomal PD-L1 Induces Systemic Anti-tumor Immunity and Memory. Cell 177, 414–427.e13. [PubMed: 30951669]

Rosenberger G, Koh CC, Guo T, Röst HL, Kouvonen P, Collins BC, Heusel M, Liu Y, Caron E, Vichalkovski A, et al. (2014). A repository of assays to quantify 10,000 human proteins by SWATH-MS. Sci Data 1, 140031. [PubMed: 25977788]

Ruggero D (2009). The Role of Myc-Induced Protein Synthesis in Cancer. Cancer Research 69, 8839–8843. [PubMed: 19934336]

Sahoo S, Klychko E, Thorne T, Misener S, Schultz KM, Millay M, Ito A, Liu T, Kamide C, Agrawal H, et al. (2011). Exosomes from human CD34(+) stem cells mediate their proangiogenic paracrine activity. Circulation Research 109, 724–728. [PubMed: 21835908]

Santangelo L, Giurato G, Cicchini C, Montaldo C, Mancone C, Tarallo R, Battistelli C, Alonzi T, Weisz A, and Tripodi M (2016). The RNA-Binding Protein SYNCRIP Is a Component of the Hepatocyte Exosomal Machinery Controlling MicroRNA Sorting. Cell Reports 17, 799–808. [PubMed: 27732855]

Sardiello M, Palmieri M, di Ronza A, Medina DL, Valenza M, Gennarino VA, Di Malta C, Donaudy F, Embrione V, Polishchuk RS, et al. (2009). A Gene Network Regulating Lysosomal Biogenesis and Function. Science 325, 473–477. [PubMed: 19556463]

Sousa D, Lima RT, and Vasconcelos MH (2015). Intercellular Transfer of Cancer Drug Resistance Traits by Extracellular Vesicles. Trends in Molecular Medicine 21, 595–608. [PubMed: 26432017]

Stine ZE, Walton ZE, Altman BJ, Hsieh AL, and Dang CV (2015). MYC, Metabolism, and Cancer. Cancer Discovery 5, 1024–1039. [PubMed: 26382145]

Strohecker AM, and White E (2014). Autophagy promotes BrafV600E-driven lung tumorigenesis by preserving mitochondrial metabolism. Autophagy 10, 384–385. [PubMed: 24362353]

Thery C, Amigorena S, Raposo G, and Clayton A (2006). Isolation and characterization of exosomes from cell culture supernatants and biological fluids. Current Protocols in Cell Biology Chapter 3, Unit 3.22.

Trajkovic K, Hsu C, Chiantia S, Rajendran L, Wenzel D, Wieland F, Schwille P, Brugger B, and Simons M (2008). Ceramide triggers budding of exosome vesicles into multivesicular endosomes. Science (New York, N.Y.) 319, 1244–1247.

Villarroya-Beltri C, Gutiérrez-Vázquez C, Sánchez-Cabo F, Pérez-Hernández D, Vázquez J, Martin-Cofreces N, Martinez-Herrera DJ, Pascual-Montano A, Mittelbrunn M, and Sánchez-Madrid F (2013). Sumoylated hnRNPA2B1 controls the sorting of miRNAs into exosomes through binding to specific motifs. Nat Commun 4, 2980. [PubMed: 24356509]

Villarroya-Beltri C, Baixauli F, Mittelbrunn M, Fernandez-Delgado I, Torralba D, Moreno-Gonzalo O, Baldanta S, Enrich C, Guerra S, and Sanchez-Madrid F (2016). ISGylation controls exosome secretion by promoting lysosomal degradation of MVB proteins. Nature Communications 7, 13588.

van de Vlekkert D, Demmers J, Nguyen X-X, Campos Y, Machado E, Annunziata I, Hu H, Gomero E, Qiu X, Bongiovanni A, et al. (2019). Excessive exosome release is the pathogenic pathway linking a lysosomal deficiency to generalized fibrosis. Sci. Adv 5, eaav3270. [PubMed: 31328155]

Wang D, Qiu C, Zhang H, Wang J, Cui Q, and Yin Y (2010). Human microRNA oncogenes and tumor suppressors show significantly different biological patterns: from functions to targets. PloS One 5, 10.1371/journal.pone.0013067.

Wollert T, and Hurley JH (2010). Molecular mechanism of multivesicular body biogenesis by ESCRT complexes. Nature 464, 864–869. [PubMed: 20305637]

Yuan TL, and Cantley LC (2008). PI3K pathway alterations in cancer: variations on a theme. Oncogene 27, 5497–5510. [PubMed: 18794884]

Zhang H, Freitas D, Kim HS, Fabijanic K, Li Z, Chen H, Mark MT, Molina H, Martin AB, Bojmar L, et al. (2018a). Identification of distinct nanoparticles and subsets of extracellular vesicles by asymmetric flow field-flow fractionation. Nat Cell Biol 20, 332–343. [PubMed: 29459780]

Zhang Q, Jeppesen DK, Higginbotham JN, Beckler MD, Poulin EJ, Walsh AJ, Skala MC, McKinley ET, Manning HC, Hight MR, et al. (2018b). Mutant KRAS Exosomes Alter the Metabolic State of

Recipient Colonic Epithelial Cells. Cellular and Molecular Gastroenterology and Hepatology 5, 627–629.e6. [PubMed: 29930982]

Zhang Q, Higginbotham JN, Jeppesen DK, Yang Y-P, Li W, McKinley ET, Graves-Deal R, Ping J, Britain CM, Dorsett KA, et al. (2019). Transfer of Functional Cargo in Exomeres. Cell Reports 27, 940–954.e6. [PubMed: 30956133]

Zhou W, Fong MY, Min Y, Somlo G, Liu L, Palomares MR, Yu Y, Chow A, O'Connor ST, Chin AR, et al. (2014). Cancer-secreted miR-105 destroys vascular endothelial barriers to promote metastasis. Cancer Cell 25, 501–515. [PubMed: 24735924]

Zimmerberg J, and Kozlov MM (2006). How proteins produce cellular membrane curvature. Nature Reviews.Molecular Cell Biology 7, 9–19. [PubMed: 16365634]

Highlights

- Oncogenes regulate cellular biomass release through the number and size of EVs
- Oncogenes alter EV protein composition and secreted miRNAs
- Ceramide metabolism is a key regulator of EV production in MYC overexpressing cells
- Downregulation of lysosome genes & activity is associated with increased EV release

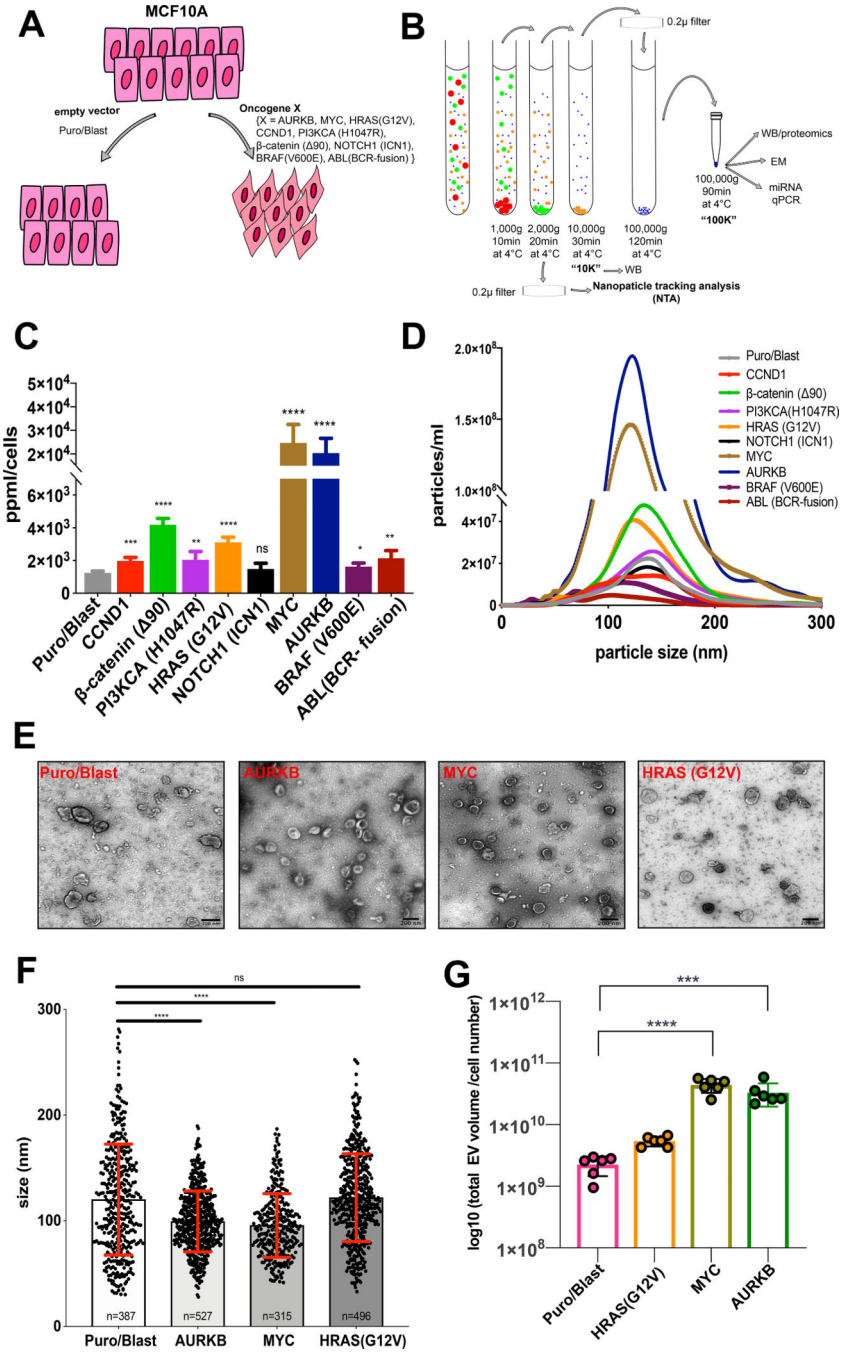

Figure 1. Oncogenes alter abundance and size of released EVs.

(A) Overview of MCF10A isogenic cell line system.

(B) Schema of EV isolation protocol and analysis.

(C) NTA of EVs isolated from MCF10A oncogenic lines. Particle per ml (ppml) counts normalized to cell number (ppml/cells) for each oncogenic line. n=6, mean±SD, unpaired two-tailed t-test between Puro/Blast and each oncogene, ns $p>0.05$, * $p<0.05$, ** $p< 0.01$, *** $p<0.001$, **** $p<0.0001$.

(D) Size distribution of EVs, mean of 6 different analysis (panel C) are plotted.

(E) Transmission electron micrograph (TEM) of 100K fractions of MCF10A oncogenic lines. Scale bar 200nm.

(F) Size quantification of 100K fractions from TEM images. Number of analyzed EVs is shown below each bar, mean±SD, unpaired two-tailed t-test between Puro/Blast and each oncogene, ns $p>0.05$, ****$p<0.0001$.

(G) The biomass loss was calculated as total volume of released EVs using a spherical model and normalized to cell number using NTA from panel C and D. n=6, mean±SD, unpaired two-tailed t-test between Puro/Blast and each oncogene, *** $p<0.001$, **** $p<0.0001$. See FigureS1 for details.

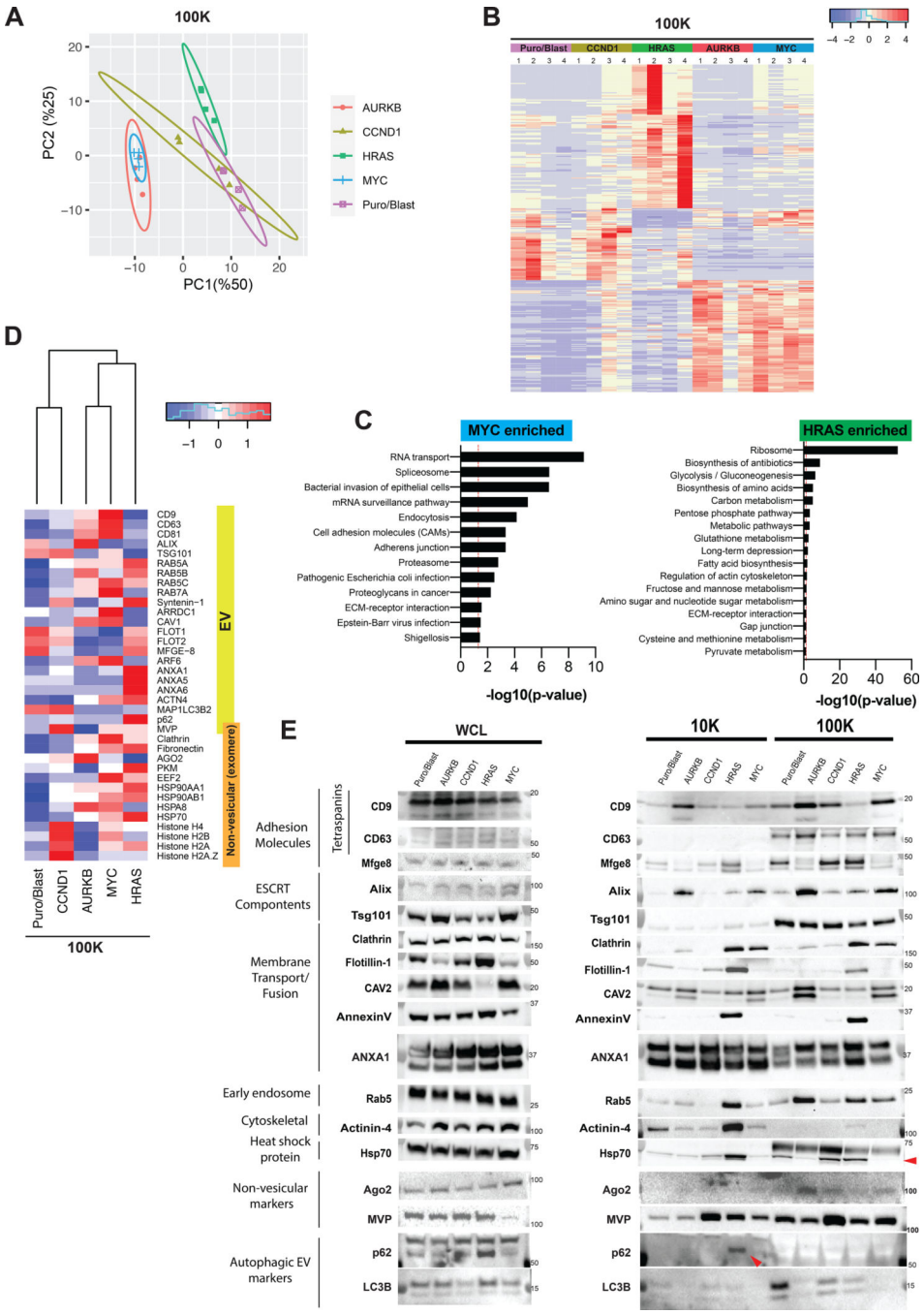

Figure 2. Oncogenes alter protein composition of EVs

(A) PCA of significantly different proteins from the 100K fractions of MCF10A oncogenic lines.

(B) Heatmap of significantly different proteins from 100K fractions, n=4 biological replicates. Scale is the normalized exclusive intensity subtracted by mean and divided by row standard deviation (i.e., Δ (area − mean)/SD).

(C) KEGG pathway analysis of enriched proteins from MYC and HRAS 100K fractions.

(D) Heatmap of commonly used EV and NV fraction markers. Average intensities of each condition are used. Scale is calculated same as in B.
(E) WB of selected EV and NV markers on whole cell lysates (WCL) on the left, the 10K and 100K fractions on the right. Red arrow indicates expected band size. Quantification of three independent experiments is in Figure S2.

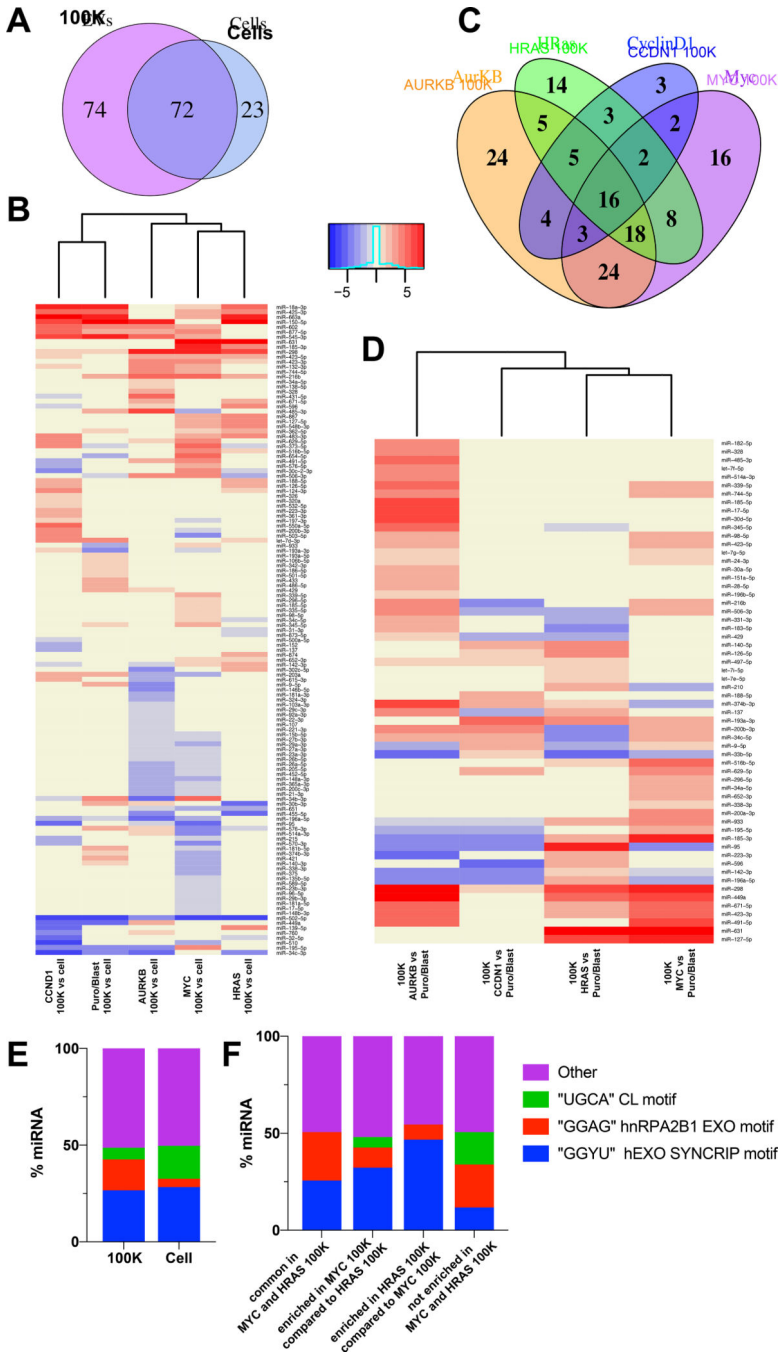

Figure 3. Oncogenes alter secreted miRNA composition

(A) Venn diagram of significantly up and down regulated miRNAs in the 100K fraction and cells from AURKB, CCND1, HRAS(G12V) and MYC overexpressing MCF10As.

(B) Heatmap of altered miRNAs in the 100K fraction versus corresponding cells. Upregulated miRNAs in 100K fractions are in red, downregulated ones are in red. See Table S2 for details.

(C) Venn diagram of miRNAs in oncogenic 100K fractions that are significantly altered compared to control 100K fraction. See Table S3 for details.

(D) The upregulated miRNAs compared to control 100K fraction in at least one of the oncogenic fractions.
(E) Histogram showing the percentage of miRNAs with known motifs in cell vs 100K.
(F) Histogram showing the percentage of miRNAs with known motifs in HRAS(G12V) and MYC 100K fractions. See Table S4 for details.

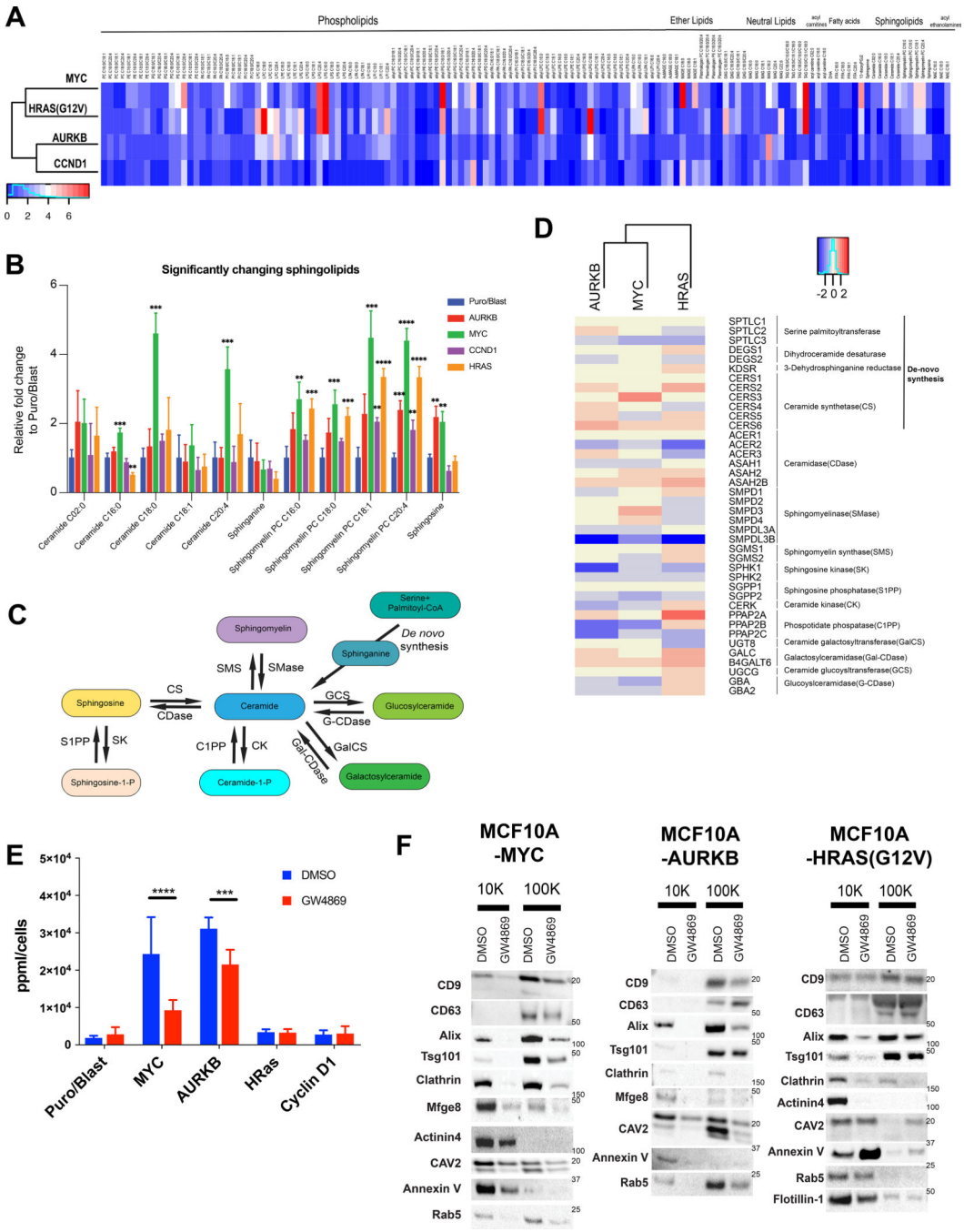

Figure 4. MYC overexpression alters ceramide metabolism and results in high number of EV release

(A) Heatmap shows relative oncogene vs control ratios of metabolites. See Table S6 for details.

(B) Relative fold change compared to control cells for sphingolipids. Mean±SEM, n=5 per group, Puro/Blast average is used for normalization. Dunnett's multiple comparison test, **p< 0.01, ***p<0.001, ****p<0.0001.

(C) Schema of ceramide biogenesis.

(D) Heatmap of altered genes in the ceramide metabolism from RNA-seq.

(E) NTA of EVs from MCF10A cells either treated with vehicle (DMSO) or GW4869 (5μM) for 48 hours. n≥5, unpaired two-tailed t-test between vehicle and treatment, ***p<0.001, ****p<0.0001.

(F) Representative blots of EV markers on 10K and 100K fractions from MCF10A cells that are either treated with DMSO or GW4869. See also Figure S3.

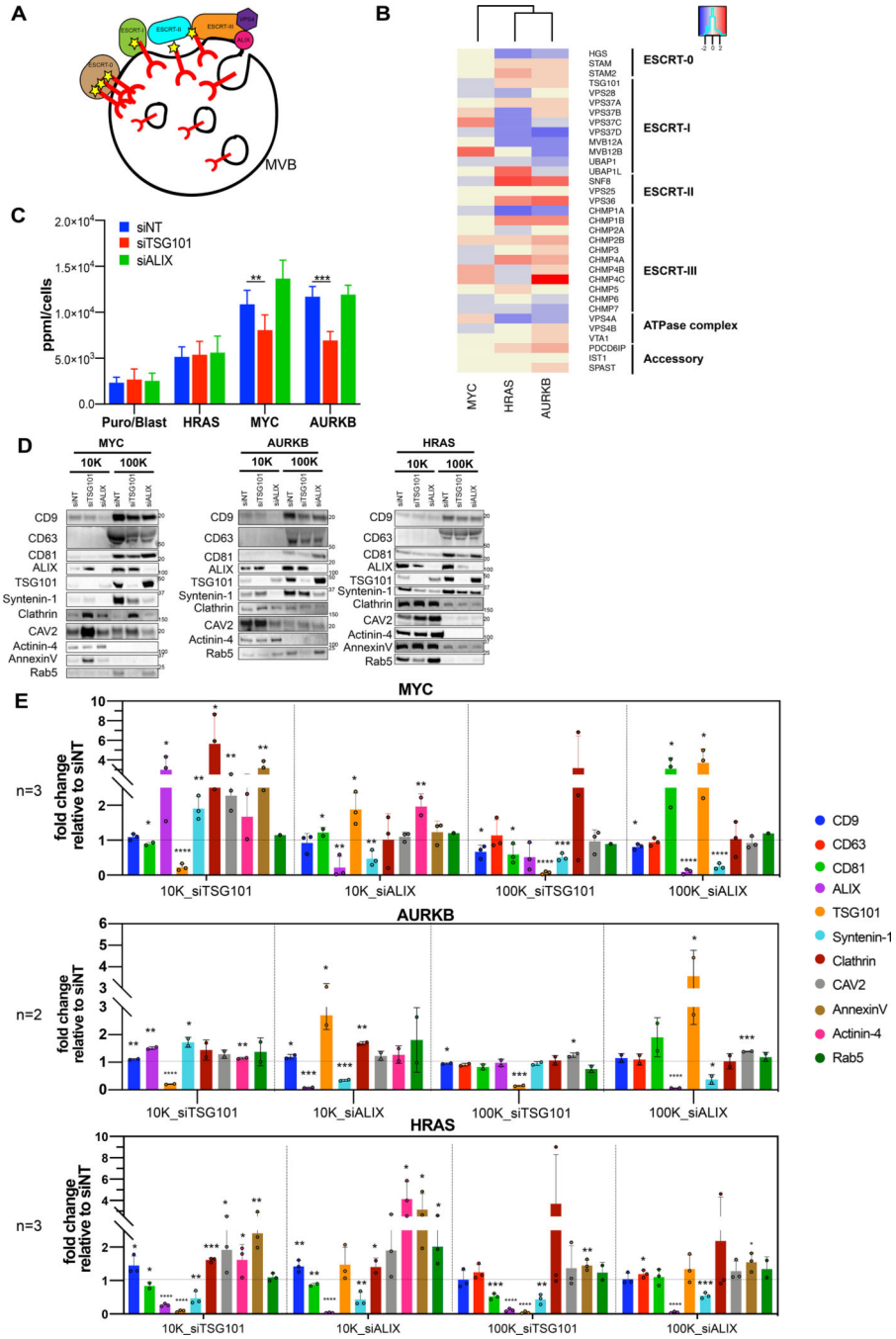

Figure 5. TSG101 is required for increased EV production in AURKB and MYC cells.

(A) Schema of ESCRT-dependent ILV budding in MVBs.

(B) Heatmap of dysregulated genes in ESRCT pathway from RNA-seq.

(C) NTA of EVs from MCF10A cells that are transfected with siRNA pools of non-targeting (siNT), TSG101 (siTSG101), and ALIX (siALIX). n=3, unpaired two-tailed t-test, **p<0.01, ***p<0.001

(D) Representative western blots of EV markers on 10K and 100K fractions from MCF10A cells that are transfected with siRNA pools.

(E) Quantification of blots from D. Fold change of EV markers relative to siNT treatment in each group compared, unpaired two-tailed t-test, *p< 0.05, **p< 0.01, ***p<0.001, ****p<0.0001

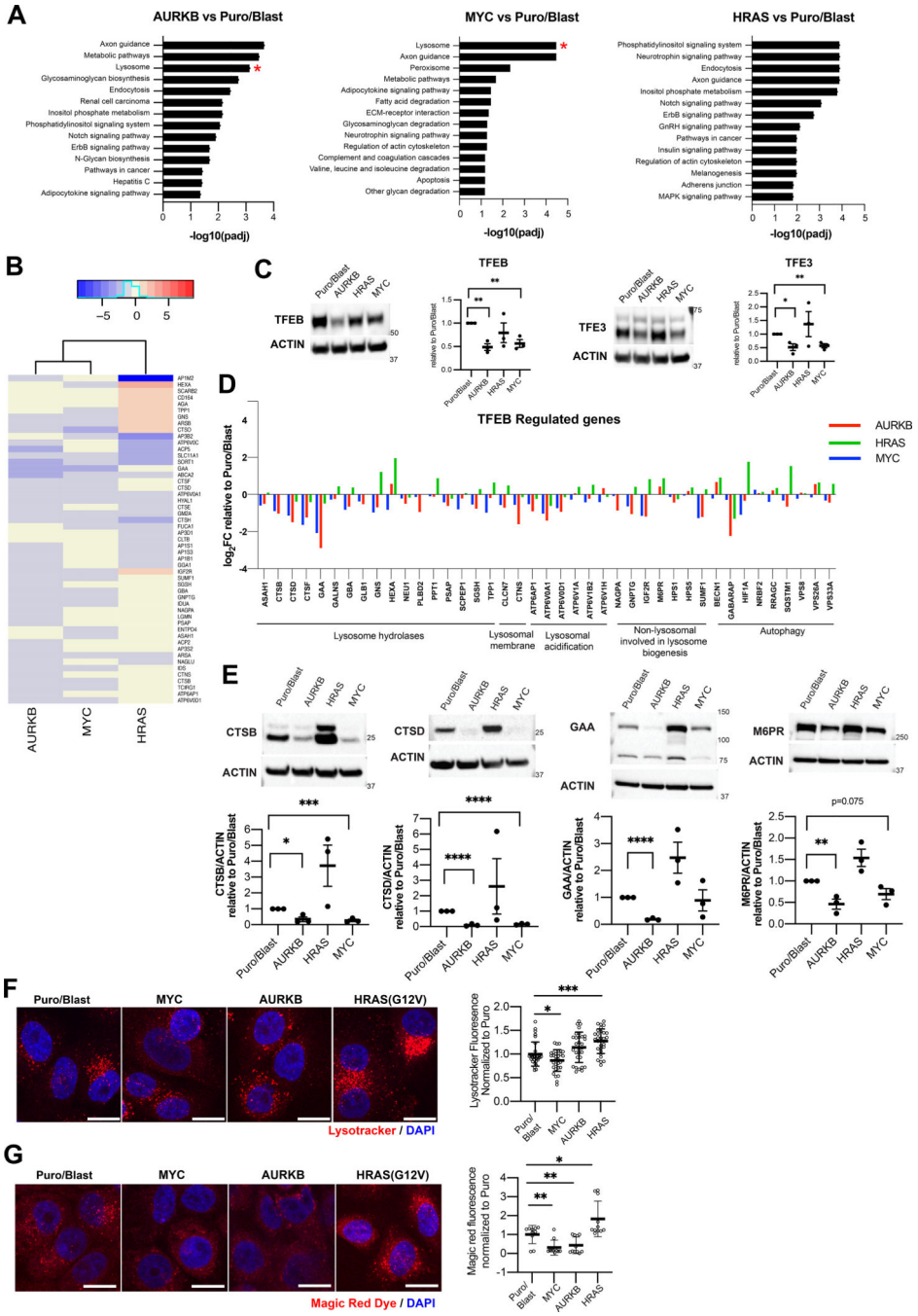

Figure 6. Downregulation of lysosome-associated genes is correlated with increased EV release.

(A) KEGG pathway analysis of downregulated pathways.

(B) Heatmap of downregulated lysosome-associated genes from RNA-seq.

(C) Western blots for TFEB and TFE3. Represented images from 3 different experiment are on the left, the quantifications are on the right. Mean±SEM, unpaired two-tailed t-test, * p<0.05, **p< 0.01, ****p<0.0001.

(D) Fold change in expression levels of TFEB regulated autophagy-lysosome genes in MYC, AURKB, and HRAS cells relative to control cells from RNA-seq.

(E) Western blots of lysosomal enzymes, CTSB, CTSD, GAA and lysosomal transport protein M6PR. Represented images from 3 different experiments are on the top, the quantifications are on the bottom. Mean±SEM, unpaired two-tailed t-test, * $p<0.05$, **$p<0.01$, *** $p<0.001$, ****$p<0.0001$.
(F) Lysotracker staining of MCF10A cell lines, scale bar 20μm. Graph on the right is the quantification of normalized fold change in lysotracker fluorescence, n=30 fields analyzed per cell line, mean±SD, unpaired t-test, * $p<0.05$, ***$p< 0.001$.
(G) Magic red staining of MCF10A cell lines, scale bar 20μm. Graph on the right is the quantification of normalized fold change in magic red fluorescence, n=10 fields analyzed per cell line, mean±SD, unpaired t-test, * $p<0.05$, **$p< 0.01$.

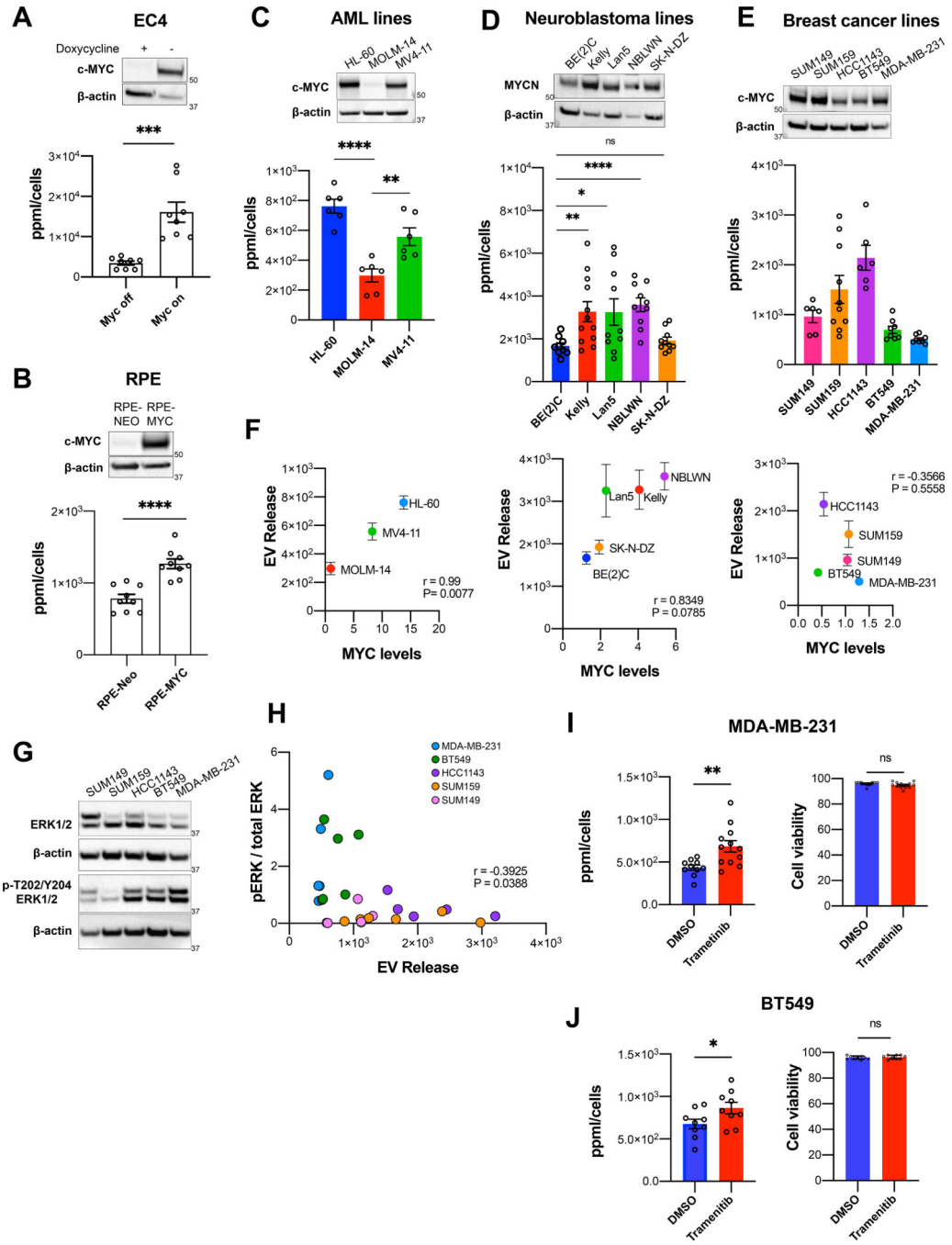

Figure 7. MYC overexpression alters EV production in other cell types but having multiple oncogenic drivers in tumors affect the EV outcome.

(A-E) sEV release from various cancer lines, immunoblot for MYC/MYCN is at the top, NTA is at bottom of the panel. **A.** EC4, mean±SEM for n=8, unpaired two-tailed t-test, *** p=0.0002. **B.** RPE cells, mean±SEM, n=9, unpaired two-tailed t-test, **** p<0.0001. **C.** AML lines, mean±SEM for n=6, unpaired two-tailed t-test, ** p< 0.01, **** p<0.0001. **D.** Neuroblastoma cell lines, mean±SEM for n≥10, unpaired two-tailed t-test, * p<0.05, ** p< 0.01, **** p<0.0001. **E.** TNBC lines, mean±SEM for n≥6 sample.

(F) Correlation between MYC levels and EV release from AML in **C**, neuroblastoma in **D** and TNBC lines in **E**. Pearson correlation and two-tailed t-test were used to generate the correlation coefficient and associated p-value.

(G) Representative image of ERK and p-ERK levels in TNBC lines.

(H) Correlation between p-ERK/total ERK levels and EV release from TNBC lines. Pearson correlation and two-tailed t-test were used to generate the correlation coefficient and associated p-value.

(I) NTA of MDA-MB-231 cells treated with 50nM MEK inhibitor, trametinib. Mean±SEM for n=12, unpaired two-tailed t-test, ** $p < 0.01$. Cell viability is on the right.

(J) NTA of BT549 cells treated with 5μM trametinib. Mean±SEM for n=9 sample, unpaired two-tailed t-test, * $p < 0.05$. Cell viability is on the right.

KEY RESOURCES TABLE

REAGENT or RESOURCE	SOURCE	IDENTIFIER
Antibodies		
Mouse anti-CD9 antibody, clone MM2/57	Millipore	Cat# CBL162; RRID: AB_2075914
Mouse anti-CD63 monoclonal antibody, Clone H5C6	BD Biosciences	Cat# 556019; RRID: AB_396297
Mouse anti-CD81 monoclonal antibody, Clone B-11	Santa Cruz Biotechnology	Cat# sc-166029; RRID: AB_2275892
Mouse anti-Human Mfg-e8 monoclonal antibody, Clone 278901	R and D Systems	Cat# MAB2767; RRID: AB_214246
Mouse anti-Alix (3A9) monoclonal antibody	Cell Signaling Technology	Cat# 2171; RRID: AB_2299455
Mouse anti-TSG101 monoclonal antibody [4A10]	Abcam	Cat# ab83; RRID: AB_306450
Rabbit anti-Clathrin Heavy Chain (D3C6) monoclonal antibody	Cell Signaling Technology	Cat# 4796; RRID: AB_10828486
Mouse anti-Flotillin-1 monoclonal Antibody, Clone 18	BD Biosciences	Cat# 610820; RRID: AB_398139
Rabbit anti-Caveolin-2 (D4A6) monoclonal Antibody	Cell Signaling Technology	Cat# 8522
Rabbit anti-Annexin V Antibody	Cell Signaling Technology	Cat# 8555; RRID: AB_10950499
Rabbit monoclonal anti-Annexin A1	Abcam	Cat# ab214486
Rabbit anti-Rab5 monoclonal antibody, Clone C8B1	Cell Signaling Technology	Cat# 3547; RRID: AB_2300649
Rabbit anti-alpha Actinin 4 antibody [C2C3]	GeneTex	GTX101669; RRID: AB_10617403
Rabbit anti-HSP70 Antibody	Cell Signaling Technology	Cat# 4872; RRID: AB_2279841
Rabbit anti-Argonaute 2 monoclonal antibody, Clone C34C6	Cell Signaling Technology	Cat# 2897; RRID: AB_2096291
Rabbit monoclonal anti-MVP	Abcam	Cat# ab175239
Guinea pig anti-p62 polyclonal antibody	Progen	Cat# GP62-C; RRID: AB_2687531
Rabbit anti-LC3B (D11) monoclonal antibody	Cell Signaling Technology	Cat# 3868; RRID: AB_2137707
Mouse anti-Human SDCBP monoclonal antibody, Clone 2C12	Abnova	Cat# H00006386-M01; RRID: AB_463981
Rabbit anti-TFEB Antibody	Cell Signaling Technology	Cat# 4240; RRID: AB_11220225
Rabbit anti-TFE3 Antibody	Cell Signaling Technology	Cat# 14779; RRID: AB_2687582
Mouse monoclonal anti-β-Actin, HRP conjugated	Santa Cruz Biotechnology	Cat# sc-47778; RRID: AB_2714189
Rabbit anti-Cathepsin B (D1C7Y) antibody	Cell Signaling Technology	Cat# 31718; RRID: AB_2687580
Mouse monoclonal anti-Cathepsin D(C-5)	Santa Cruz Biotechnology	Cat# sc-377124; Lot# EO819
Rabbit monoclonal anti-GAA antibody [EPR4716(2)]	Abcam	Cat# ab137068; RRID: AB_2687584
Rabbit monoclonal anti-Mannose 6 Phosphate Receptor (Cation independent) antibody [EPR6599]	Abcam	Cat# ab124767; RRID: AB_10974087
Rabbit monoclonal [Y69] to c-Myc, HRP conjugated	Abcam	Cat# ab205818
Mouse monoclonal anti-n-MYC/MYCN antibody	Abcam	Cat# ab16898; RRID: AB_443533

REAGENT or RESOURCE	SOURCE	IDENTIFIER
Rabbit anti-p44/42 MAPK (Erk1/2) antibody	Cell Signaling Technology	Cat# 9102; RRID: AB_330744
Mouse anti-Phospho-p44/42 MAPK (Erk1) (Tyr204)/(Erk2) (Tyr187) (D1H6G) monoclonal antibody	Cell Signaling Technology	Cat# 5726; RRID: AB_2797617
Mouse monoclonal anti-Histone, H1 + core proteins, clone F152.C25.WJJ antibody	Millipore	Cat# MABE71; RRID: AB_10845941
Rat anti-Grp94 monoclonal (9G10) antibody	Enzo Life Sciences	Cat# ADI-SPA-850; RRID: AB_10615091
Mouse anti-Cytochrome C monoclonal antibody, Clone 7H8.2C12	BD Biosciences	Cat# 556433; RRID: AB_396417
Mouse monoclonal anti-HSPA13 (STCH)	Santa Cruz Biotechnology	Cat# sc-398297
Rabbit anti-PKM1 (D30G6) monoclonal antibody	Cell Signaling Technology	Cat# 7067; RRID: AB_2715534
Goat anti-mouse IgG-HRP antibody	Santa Cruz Biotechnology	Cat# sc-2055; RRID: AB_631738
Goat anti-rabbit IgG, HRP-linked antibody	Cell Signaling Technology	Cat# 7074; RRID: AB_2099233
Rabbit anti-Guinea Pig IgG (H+L) secondary antibody, HRP	Thermo Fisher Scientific	Cat# 61–4620; RRID: AB_2533926
Goat anti-rat IgG-HRP antibody	Santa Cruz Biotechnology	Cat# sc-2303; RRID: AB_650501
Chemicals, peptides, and recombinant proteins		
Knockout Serum Replacement (KSR)	Life Technologies	Cat# 10828028
OptiPrep Density Gradient Medium	Sigma-Aldrich	Cat# D1556
Lysotracker Red DND-99	Thermo Fisher Scientific	Cat# L7528
Magic Red Cathepsin B Assay	Immunochemistry Technologies	Cat # 938
DAPI Fluoromount-G	Southern Biotech	Cat# 0100–20
GW4869	Sigma-Aldrich	Cat# D1692
Trametinib	Selleck Chemicals	Cat# S2673
Trypan Blue Stain	Thermo Fisher	Cat# T10282
Lipofectamine RNAiMAX Transfection Reagent	Thermo Fisher	Cat# 13778075
cOmplete™, Mini, EDTA-free Protease Inhibitor Cocktail	Millipore	Cat# 11836170001
PhosSTOP **phosphatase inhibitor tablets**	Millipore	Cat# 4906845001
Visualizer™ Western Blot Detection Kit	Millipore	Cat# 64–202BP
Critical commercial assays		
RNeasy Micro Kit	Qiagen	Cat# 74004
Universal cDNA Synthesis Kit II	Exiqon	Cat# 203301
Deposited data		
RNA sequencing data	This paper	GEO: GSE130768
Proteomics data	This paper	PXD025445; MassIVE MSV000087219
Experimental models: cell lines		
Human: MCF10A Puro/Blast (Control)	Andrei Goga, UCSF, Martins M. et. al., 2015	N/A
Human: MCF10A AURKB	Andrei Goga, UCSF, Martins M. et. al., 2015	N/A

REAGENT or RESOURCE	SOURCE	IDENTIFIER
Human: MCF10A CCDN1	Andrei Goga, UCSF, Martins M. et. al., 2015	N/A
Human: MCF10A HRAS(G12V)	Andrei Goga, UCSF, Martins M. et. al., 2015	N/A
Human: MCF10A MYC	Andrei Goga, UCSF, Martins M. et. al., 2015	N/A
Human: MCF10A β-catenin	Andrei Goga, UCSF, Martins M. et. al., 2015	N/A
Human: MCF10A BRAF	Andrei Goga, UCSF, Martins M. et. al., 2015	N/A
Human: MCF10A NOTCH1	Andrei Goga, UCSF, Martins M. et. al., 2015	N/A
Human: MCF10A PIK3CA (H1047R)	Andrei Goga, UCSF, Martins M. et. al., 2015	N/A
Human: MCF10A ABL(BCR-fusion)	Andrei Goga, UCSF, Martins M. et. al., 2015	N/A
Mouse: EC4	Dean Felsher, Stanford University	N/A
Human: RPE-Neo	Andrei Goga, UCSF, Goga et. al., 2007	N/A
Human: RPE-MYC	Andrei Goga, UCSF, Goga et. al., 2007	N/A
Human: HL-60	ATCC	Cat# CCL-240; RRID: CVCL_0002
Human: MOLM-14	Scott Kogan, UCSF	N/A
Human: MV4–11	Scott Kogan, UCSF	N/A
Human: BE(2)C	Weiss Lab, UCSF, Swarbrick A. et. al. 2010	N/A
Human: Kelly	Weiss Lab, UCSF, Swarbrick A. et. al. 2010	N/A
Human: Lan5	Weiss Lab, UCSF, Swarbrick A. et. al. 2010	N/A
Human: NBLWN	Weiss Lab, UCSF, Swarbrick A. et. al. 2010	N/A
Human: SK-N-DZ	Weiss Lab, UCSF, Swarbrick A. et. al. 2010	N/A
Human: SUM149	BIOIVT	RRID: CVCL_3422
Human: SUM159	BIOIVT	RRID: CVCL_5423
Human: HCC1143	ATCC	Cat# CRL-2321; RRID: CVCL_1245
Human: BT549	ATCC	Cat# HTB122; RRID: CVCL_1092
Human: MDA-MB-231	ATCC	Cat# HTB-26; RRID: CVCL_0062
Oligonucleotides		
ON-TARGET plus Human TSG101 siRNA, SMART pool	Dharmacon	Cat# L-003549-00-0005
ON-TARGET plus Human PDCD6IP siRNA, SMART pool	Dharmacon	Cat# L-004233-00-0005
ON-TARGET plus Non-targeting pool	Dharmacon	Cat# D-001810-10-05
miRCURY LNA miRNA Human Panel I	Qiagen	Cat# YAHS-301YE-4
Software and algorithms		
Fiji	Schindelin et. al., 2012	https://fiji.sc/

REAGENT or RESOURCE	SOURCE	IDENTIFIER
Image Lab 6.1	BioRad	https://www.bio-rad.com/en-us/product/image-lab-software?ID=KRE6P5E8Z
Scaffold DIA v.2.0.0	Proteome Software	https://www.proteomesoftware.com
GenEX	MultiD	https://multid.se/genex/
DESeq2	Bioconductor	https://bioconductor.org/packages/release/bioc/html/DESeq2.html
R	The R Foundation	https://www.r-project.org
Prism 9	Graphpad	https://www.graphpad.com
DAVID Bioinformatics Resource	Huang et al., 2008, 2009	https://david.ncifcrf.gov/